TECHNICAL MEMORANDUM

X-416

A COLD-FLOW INVESTIGATION OF JET-INDUCED THRUST-VECTOR CONTROL

By John E. McAulay and Albert J. Pavli

Lewis Research Center
Cleveland, Ohio

NATIONAL AERONAUTICS AND SPACE ADMINISTRATION

WASHINGTON

December 1960

NATIONAL AERONAUTICS AND SPACE ADMINISTRATION

TECHNICAL MEMORANDUM X-416

A COLD-FLOW INVESTIGATION OF JET-INDUCED THRUST-VECTOR CONTROL*

By John E. McAulay and Albert J. Pavli

SUMMARY

An experimental program has been conducted to investigate several methods of obtaining thrust-vector control by introducing a secondary gas into the primary-nozzle flow field. These methods were evaluated in a cold-flow rig using a bell-shaped nozzle having an expansion ratio of 7.27. The data were obtained over a range of secondary flows at or near the primary-nozzle design pressure ratio.

The radial injection method produced a maximum amplification ratio of 1.3 using a single convergent port located at a primary-nozzle expansion ratio of about 6. Maximum amplification ratios between 2.3 and 2.9 were achieved with the counterstream injection method depending on the position of the counterstream nozzle and on the secondary-flow ratio. (Amplification ratio is defined as the ratio of vector force to primary thrust divided by the ratio of secondary to primary flow.) Other methods, such as tangential, slanted-tube, and throat injection, gave relatively poor maximum amplification ratios (i.e., 0.8 or less).

INTRODUCTION

A number of methods have been proposed and several used to provide thrust-vector control to rocket-powered vehicles. The methods which have been used extensively up to the present are the gimbaled engine or nozzle, jet vanes, jetavators, and aerodynamic surfaces. Except for the last case vector control is provided by turning the rocket jet so as to create a moment about the center of gravity of the missile. Each method, of course, has certain recognized advantages and disadvantages, and the choice of one scheme over the other depends to a large extent on its development status and the particular application.

Another method has been proposed and is referred to herein as jet-induced thrust-vector control. This method produces a force perpendicular to the primary thrust by injecting a secondary gas into the primary-nozzle flow field so as to turn or deflect the primary flow. The advantages of this method can be realized particularly when the missile requirements

*Title, Unclassified.

include one or more of the following: (1) vector control of large solid-propellant rockets, (2) fast control response, or (3) vector control requiring small secondary total impulse relative to the total impulse of the missile.

The preliminary investigation reported herein was conducted at the NASA Lewis Research Center to determine the cold-flow performance of several jet-induced thrust-vector control configurations. The configurations examined may be divided into two broad categories: (1) those injecting the secondary gas through ports or nozzles in the wall of the primary nozzle (ref. 1) and (2) those applying the new concept of injecting the secondary gas upstream (i.e., counterstream) into the primary-nozzle exit. All the data reported herein were obtained using a bell-shaped primary nozzle having an expansion ratio of 7.27. Performance data are presented showing the effect of a number of injection variables, including injection location, secondary Mach number, and secondary-flow orientation with respect to the primary-nozzle flow. (Symbols are defined in appendix A, and methods of calculation are given in appendix B.) No attempt has been made to evaluate the reliability and overall missile performance using the systems studied.

APPARATUS

Installation and Instrumentation

The nozzle rig is shown installed in the altitude test chamber in figures 1 and 2. The primary air was supplied to the test nozzle at a pressure of about 90 pounds per square inch absolute from a duct connected to the nozzle rig by a frictionless labyrinth seal. Secondary air up to a maximum pressure of about 135 pounds per square inch absolute was supplied by a separate piping arrangement to the secondary ports or nozzles through the system illustrated in figure 2. In the case of the high-pressure counterstream configuration, the secondary gas was nitrogen (at approx. 1500 lb/sq in.), which was supplied to the counterstream nozzles directly from bottle storage. The nominal temperature of both the air and the nitrogen was 550° R.

The test nozzle and its associated ducting were attached to the bedplate by a rigid trunnion strut and a flexure strain-gage link. The nozzle and ducting were only restrained in the pitch direction about the trunnion mount by the strain gage, which was devised to measure vector force. The bedplate was in turn supported by flexure rods and was restrained in the axial direction by the primary thrust-measuring cell. Although the flexible lines in the secondary air system did not remain flexible when highly pressurized, the sensitivity of the primary thrust cell and strain gage was between 95 and 100 percent of that obtained with the secondary line not pressurized or disconnected. The effect of the secondary-line pressurization was taken into account by an extensive dead-weight calibration.

The basic primary nozzle used during this investigation was a convergent-divergent bell-shaped nozzle made of wood and having an expansion ratio of 7.27. The coordinates and area variation of this nozzle are presented in figure 3. The nozzle had a maximum turning angle of about 27° and an exit angle of 7°. The length of the divergent part of the nozzle was 80 percent of a 15° half-angle conical nozzle of the same area ratio. The nozzle flow coefficient was measured to be 0.989, and the actual- to ideal-thrust ratio at the design point (pressure ratio of about 85) was 0.987.

Pressures and temperatures were measured at the various locations in the test rig indicated in figure 2. In addition, between 46 and 53 wall static taps were available on the divergent portion of the primary nozzle (mostly near the secondary ports or nozzles). The primary thrust and the vector forces were determined, however, from a balanced-air-diaphragm cell and a strain gage, respectively. All pressure, temperature, and force measurements were registered on the laboratory digital automatic recorder systems.

Secondary Injection Configurations

Radial. - Schematic diagrams and photographs of the principal features of the radial injection configurations are presented in figures 4 and 5. The secondary ports were designed to produce a secondary flow perpendicular to the inside wall of the primary nozzle. Single radial injection was studied at three axial locations in the primary nozzle (fig. 4). The port being used was always alined with the vector-force strain gage by rotating the divergent portion of the primary nozzle.

Multiple injection ports (fig. 5) were investigated in groups of three or five at the same three axial locations as the single injection ports. They were also used in a group of three with one port at each axial location (called axial multiple injection configuration).

Counterstream. - A schematic diagram of the low-pressure counterstream configuration is shown in figure 6. It was possible to traverse the counterstream nozzle in the vertical direction from a fully retracted position to a point near the primary-nozzle centerline. In addition, the counterstream flow angle could be varied ±20° with respect to the primary-nozzle centerline. Counterstream nozzles having expansion ratios between 1.7 and 2.9 were investigated.

A schematic diagram and a photograph of the high-pressure counterstream configuration are presented in figure 7. This configuration was designed to provide about the same secondary flow as the low-pressure system, but at a secondary pressure 10 times greater. The traversing and flow-angle characteristics of the high pressure system were essentially the same as those of the low-pressure system just described. Secondary nozzles for this system had expansion ratios between 2.0 and 6.5.

Both counterstream configurations were installed so that jet reaction force and drag of the counterstream nozzles were an integral part of the measured primary thrust and vector force.

Tangential. - A schematic diagram giving the pertinent information on the tangential configuration is shown in figure 8. Air was injected at three axial locations. It was necessary to operate the tangential ports in pairs in order to have zero rolling moment and a predictable direction of the vector force.

Slanted tube. - Figure 9 presents a schematic diagram of the slanted-tube configuration. This configuration could be considered as a cross between the radial and counterstream configurations. The exit of the slanted tube was placed so as to be coincident with the edge of the primary-nozzle flow field.

Throat injection. - A schematic diagram of the throat injection configuration is shown in figure 10. It can be considered as a special case of radial injection.

RESULTS AND DISCUSSION

Data Reproducibility

Inasmuch as the data presented herein were the first data from this particular test rig, several checks were made to determine data reproducibility. Two sets of data separated by many runs and configuration changes are shown in figure 11, where vector-force to primary-thrust ratio F_s/F_p is plotted as a function of secondary- to primary-weight-flow ratio w_s/w_p. The data reproducibility proved to be very good. Hereafter, F_s/F_p is referred to as the vector-force ratio and w_s/w_p as the secondary-flow ratio.

Radial Secondary Injection

Typical performance with radial injection. - Typical performance for radial injection configurations is illustrated in figures 12 and 13. As the secondary-flow ratio was raised with the primary nozzle operating near the design pressure ratio (fig. 12), the primary-nozzle-thrust and the vector-force ratio increased linearly, while the amplification ratio $(F_s/F_p)/(w_s/w_p)$ remained nearly constant at 1.3. For a secondary-flow ratio of 0.06, the primary thrust was 3 percent higher than at zero secondary flow, and the vector-force ratio was 0.077. The reaction force of the secondary flow, indicated by the dashed line on the vector-force-ratio plot, accounted for about 60 percent of the total vector force. The remaining 40 percent of the total vector force was, of course, a result of the induced pressure field set up within the primary nozzle.

A typical static-pressure distribution in the primary nozzle with radial injection is presented in figure 13, where the ratio of local static pressure to primary-nozzle inlet total pressure is plotted against distance downstream of the nozzle throat. The angles given refer to the circumferential displacement from an axial plane which passes through the injection port. Along this plane the static pressure followed the normal curve as the flow proceeded toward the nozzle exit from the throat, and as the flow approached the secondary port, flow separation occurred. This flow separation produced a sizable increase in the static pressure which reached a peak near the secondary port. Beyond this point, the pressure decreased and reached values below the normal pressure at the nozzle exit. As the reference plane was moved circumferentially away from the secondary port, the pressure peaks became less pronounced and moved in a downstream direction. From these considerations, it can be visualized that a secondary-port location too far upstream in the nozzle will produce a downstream region of static pressure below normal over a large surface area. Conversely, a location too near the nozzle exit will not be effective in providing surface area in the high-pressure region.

Effect of secondary-port axial location and size. - Vector-force ratio and amplification ratio are presented as functions of secondary-flow ratio for the axial positions investigated with single large, single small, and multiple ports (fig. 14). In general, the data indicate that axial position 2 (the center position at a primary-nozzle area ratio of 5.98) was the more nearly optimum. The aft position produced the lowest vector force with the single ports, whereas the forward position produced the lowest vector force with the multiple ports. The effect of axial location of the ports on vector force was qualitatively substantiated by integration of the static-pressure distributions for both the single- and multiple-port configurations.

Comparison of figures 14(a) and (b) indicates comparable vector performance for the two sizes of single injection ports investigated. Thus, the vector performance was primarily a function of secondary-flow ratio and essentially independent of secondary- to primary-pressure ratio. Comparison of vector performance with single and multiple ports (fig. 14(c)) shows the best performance was obtained with the single ports; this is covered in more detail in the following section.

Effect of number of secondary ports at a given axial location. - Data for secondary-injection configurations consisting of one, three, and five ports at a given axial location are presented in figure 15, where vector-force and amplification ratios are plotted as functions of secondary-flow ratio. Inasmuch as axial position 2 provided the highest vector force for either single or multiple injection (figs. 14(a) and (c)), the comparison between single- and multiple-port systems is made at that position. The vector force obtained with single injection was about 10 percent greater than that with multiple injection. This trend is

associated with both the angularity of the secondary jet reaction force and the change in the induced static-pressure field as the number of secondary ports is altered.

Performance of axial multiple-port convergent and single-port convergent-divergent radial injection. - The performance of the remaining radial injection configurations investigated, namely the axial multiple-port and the convergent-divergent single-port configurations is presented in figure 16, where the vector-force and amplification ratios are shown as a function of secondary-flow ratio. As indicated previously, the axial multiple-port configuration consisted of three convergent ports in line at three axial positions. For comparison purposes, the dashed line gives the vector force obtained with the large single radial injection port at axial position 2. The vector force for the above mentioned configurations was 10 to 14 percent less than that obtained with the single convergent port. This result, in the case of the single convergent-divergent ports, is somewhat surprising; however, integration of the static-pressure distribution in the primary nozzle did lend support to these data trends.

Low-Pressure Counterstream Secondary Injection

Two expressions are used in discussing the counterstream injection which need to be clearly defined. The full-capture position is the location where the circle formed by the exit of the counterstream nozzle is tangent to and contained within the circle formed by the exit of the primary nozzle. The maximum-vector-force position is arbitrarily defined as the radial location where the maximum vector force occurred at the highest secondary-flow ratio investigated (i.e., w_s/w_p of about 0.066).

The vector force or moment produced by the counterstream injection method is a summation of several components. These are induced pressure moment acting on the primary nozzle and the reaction and drag moments of the counterstream nozzle. These latter two moments oppose that produced by the induced pressure acting on the primary nozzle.

Typical effects of counterstream-nozzle position on vector force. - The effect of counterstream-nozzle position on vector force is presented in figure 17 for a typical case, where vector-force ratio is plotted against counterstream-nozzle position for four weight-flow ratios. The counterstream-nozzle position is given in terms of the percent of travel from the full-capture position to a position at the primary-nozzle centerline. For the two higher flow ratios, 0.066 and 0.051, the vector-force ratio reached a maximum when the counterstream nozzle reached a position about 35 percent of the way between the full-capture position and the primary-nozzle centerline. At the two lower flow ratios, 0.027 and 0, the vector-force ratio was a maximum at the full-capture position.

Typical performance with counterstream injection at the full-capture and maximum-vector-force positions. - Figures 18 and 19 present typical performance with the counterstream injection for the two most pertinent positions, namely, full capture and maximum vector force. At low flow ratios the full-capture position gave the best performance (fig. 18). For example, at a secondary-flow ratio of 0.02 the amplification ratio was 2.9, while at the maximum-vector-force position the amplification ratio was nearly zero. However, at high flow ratios (0.06) the amplification ratio was 1.7 at the full-capture position compared with 2.3 for the maximum-vector-force position. It should be noted here (and it is discussed later) that the counterflow technique provides substantially larger amplification ratios than the radial injection technique discussed earlier. At very low values of secondary-flow ratio, the full-capture position produced significant vector forces; however, this condition would probably be considered impractical for essentially steady state operation because of the lack of potential cooling offered by the secondary flow. For the maximum-vector-force position, the vector forces were slightly negative at the very low flow ratios (i.e., in the reverse direction).

The effect of the counterstream nozzle and secondary flow on the primary-nozzle thrust is also shown in figure 18, where the ratio of primary thrust with secondary flow to primary thrust with the counterstream nozzle retracted and zero secondary flow is plotted as a function of secondary-flow ratio. At a flow ratio of 0.02 the primary thrust is not affected at the full-capture position but is reduced 4 percent at the maximum-vector-force position. At a flow ratio of 0.06 the corresponding values are a 2-percent increase and a 2-percent loss in primary thrust. These effects of counterstream-nozzle position and flow on primary thrust are not optimum but are associated with the particular hardware used.

Typical primary-nozzle static-pressure distributions at a secondary-flow ratio of 0.066 are presented in figure 19 for full-capture and the maximum-vector positions. Comparison of these static-pressure distributions shows that at the maximum-vector-force position higher static pressures are produced toward the primary-nozzle exit, where greater surface area per unit length exists. This, in addition to the movement of the center of pressure downstream in the nozzle, resulted in higher vector-force ratios than at the full-capture position.

Effect of counterstream-nozzle expansion ratio. - Figure 20 shows that changing the counterstream-nozzle expansion ratio from 1.7 to 2.9 had very little effect on performance. The only effect was a slight reduction in performance with the 1.7 expansion ratio nozzle at the full-capture position. The trends and magnitude of the vector forces obtained are essentially the same as exhibited in figure 18.

Effect of counterstream flow angle. - Figure 21 shows that changing the counterstream flow angle (with respect to the primary-nozzle centerline) did not significantly influence vector performance for the full-capture position. However, at the maximum-vector-force position the optimum vector performance was obtained when the flow was injected parallel to the nozzle centerline.

Performance comparison of the low- and high-pressure counterstream configurations. - In an effort to minimize the size of the counterstream nozzles and to evaluate potential performance gains, a high-pressure counterstream system was investigated. A comparison of the performance of the low- and high-pressure counterstream configurations is presented in figure 22. At the full-capture position, the low-pressure system gave higher vector-force ratios than the high-pressure system. This trend is probably associated with the respective frontal areas of the two systems. However, when the counterstream nozzle was immersed farther into the primary-flow field to the position where the maximum vector force is attained for each system, the high-pressure system produced a vector force from 12 to 17 percent greater than the low-pressure system. This result was valid over a range of counterstream-nozzle area ratios from 1.7 to 2.9 for the low-pressure system and 3.6 to 6.5 for the high-pressure system.

The change in primary thrust as counterstream-nozzle position is varied is also presented in figure 22. Near the full-capture position both the low- and high-pressure systems increased the primary thrust 3 to 4 percent above the primary thrust attained with the counterstream nozzle retracted and at zero flow. At the maximum-vector-force positions, the high-pressure system had a primary thrust about the same as the thrust attained with the counterstream nozzle retracted and at zero flow, while the low-pressure system had a primary thrust about 2 percent lower.

Effect of counterstream-nozzle expansion ratio. - The effect of counterstream-nozzle expansion ratio for the high-pressure system is presented in figure 23, where vector-force ratio is shown as a function of counterstream-nozzle position for expansion ratios from 2.0 to 6.5. The high vector-force ratio at the full-capture position for the 6.5 expansion ratio data is not particularly significant in that a wide range of values were obtained at this nozzle position (possibly because of a flow instability). Both the 6.5 and 3.6 expansion ratio nozzles gave the same performance at positions other than the full-capture position. However, the low-expansion-ratio nozzle (2.0) had a peak vector force about 16 percent lower than the larger area ratio nozzles. This probably was associated with the large amount of underexpansion of the secondary flow with this counterstream nozzle.

Effect of counterstream flow angle. - The effect of counterstream flow angle for the high-pressure counterstream system was only determined sufficiently to verify that the effect of flow angle was the same as on the low-pressure counterstream system.

Low-Performance Configurations

Several other schemes were evaluated during the course of the program, and the results are presented in figure 24 for three configurations, the tangential at three axial locations, the slanted tube, and throat injection. This latter configuration is actually a special case of radial injection. Also repeated in this figure is the performance of the best radial injection configuration. The configurations defined by the data points are from 35 to well over 100 percent lower in performance than the single-port radial injection configurations, the highest amplification ratio being 0.8.

Direct Performance Comparison of the Better Vector-Control Configurations

Curves representing the performance of the better vector-control configurations investigated are given in figure 25, where amplification ratio is shown as a function of secondary-flow ratio. The curves are for the best radial injection, the low-pressure counterstream configuration at full-capture and maximum-vector-force positions, and the high-pressure counterstream configuration at the maximum-vector-force position. The counterstream configurations with amplification ratios from 2.3 to 2.9 over a range of flow ratios and counterstream-nozzle positions had much higher aerodynamic performance than the radial configuration whose amplification ratio was 1.3. However, there are other considerations, such as installation, weight, and cooling, which must be taken into account. These factors are beyond the scope of this paper.

CONCLUDING REMARKS

A cold-flow investigation was conducted to determine the aerodynamic performance of several methods of obtaining thrust-vector control for rocket nozzles by introducing secondary flow in the primary-nozzle flow field. All the data were obtained with a bell-shaped primary nozzle having an expansion ratio of 7.27. The optimum vector force of the radial injection method was achieved with a single convergent port located at a primary-nozzle expansion ratio of about 6. This configuration produced an amplification ratio of about 1.3 over a range of secondary-flow ratios from 0.02 to 0.07. The size of the secondary port did not appreciably alter its effectiveness other than, of course, to limit the maximum secondary flow and vector force for a particular secondary total pressure.

The performance of the counterstream method was primarily a function of secondary flow and the counterstream-nozzle position. At low secondary-flow ratios (0.02) the full-capture position of the counterstream nozzle yielded the highest amplification ratio, namely, about 2.9. At high secondary-flow ratios (0.05 to 0.06) the optimum position of the low-pressure counterstream nozzle was about 35 percent of the distance

between full capture and the primary-nozzle centerline. At this location the amplification ratio was approximately 2.3. For the same secondary-flow ratios the high-pressure counterstream nozzle had an amplification ratio of about 2.7 at a position about 45 percent of the distance between full capture and the primary-nozzle centerline. Although the counterstream injection had aerodynamic performance clearly superior to the radial injection, it is believed that other considerations, such as installation, weight, and cooling, would reduce this superiority.

Other means of secondary injection, such as tangential, slanted tube, and throat injection, were evaluated and found to be low in performance, having amplification ratios of 0.8 or lower.

Lewis Research Center
National Aeronautics and Space Administration
Cleveland, Ohio, September 23, 1960

APPENDIX A

SYMBOLS

A	area, sq ft
B	thrust or vector force measured by thrust cell or strain gage, lb
C_d	flow coefficient
F_p	primary thrust, lb
F_s	vector force, lb
g	acceleration due to gravity, 32.17 ft/sec^2
P	total pressure, lb/sq ft abs
p	static pressure, lb/sq ft abs
R	gas constant, 53.4 ft-lb/(lb)($^\circ$R)
T	total temperature, $^\circ$R
V	velocity, ft/sec
w	gas flow, lb/sec
γ	ratio of specific heats

Subscripts:

link	thrust member
p	primary
s	secondary or vector
seal	labyrinth seal
t	throat
x	constant-area inlet duct to Venturi meter
0	ambient
1	primary-airflow measuring station (Venturi meter)
2	primary-nozzle inlet

APPENDIX B

METHODS OF CALCULATION

Primary airflow. - The primary-nozzle airflow was calculated by measurements taken at a Venturi measuring station (station 1) as follows:

$$w_p = C_{d,1} p_1 A_1 \sqrt{\frac{2\gamma_1 g}{(\gamma_1 - 1)RT_1}\left(\frac{P_1}{p_1}\right)^{\frac{\gamma_1-1}{\gamma_1}}\left[\left(\frac{P_1}{p_1}\right)^{\frac{\gamma_1-1}{\gamma_1}} - 1\right]} \qquad (1)$$

Secondary airflow. - The secondary airflow was calculated by measurements taken at an orifice measuring station in the secondary air line. The following equations are applicable for two orifice sizes:

$$w_s = 0.03822\left[1 - 0.2949\left(\frac{p_{s,1} - p_{s,2}}{p_{s,1}}\right)\right]\left(\frac{p_{s,1}}{\sqrt{RT_s}}\right)\left(\frac{p_{s,1} - p_{s,2}}{p_{s,1}}\right)^{1/2} \qquad (2a)$$

$$w_s = 0.1804\left[1 - 0.3301\left(\frac{p_{s,1} - p_{s,2}}{p_{s,1}}\right)\right]\left(\frac{p_{s,1}}{\sqrt{RT_s}}\right)\left(\frac{p_{s,1} - p_{s,2}}{p_{s,1}}\right)^{1/2} \qquad (2b)$$

where $p_{s,1}$ is the absolute pressure upstream of the orifice and $p_{s,2}$ is the absolute pressure downstream of the orifice.

Primary thrust. - The primary-nozzle thrust was determined from the following equation:

$$F_p = B_p + A_{seal}(P_1 - p_0) + A_{link}(2050 - p_0) + \frac{w_p}{g} V_x \qquad (3)$$

where constants involved in determining B_p, A_{seal}, and A_{link} were evaluated during calibration runs.

Vector force. - The vector force produced by the secondary system was determined from the following expression:

$$F_s = KB_s \qquad (4)$$

where K is a calibration constant.

REFERENCE

1. Lingen, A.: Jet-Induced Thrust-Vector Control Applied to Nozzles Having Large Expansion Ratios. Rep. R-0937-33, United Aircraft Corp., Mar. 1, 1957.

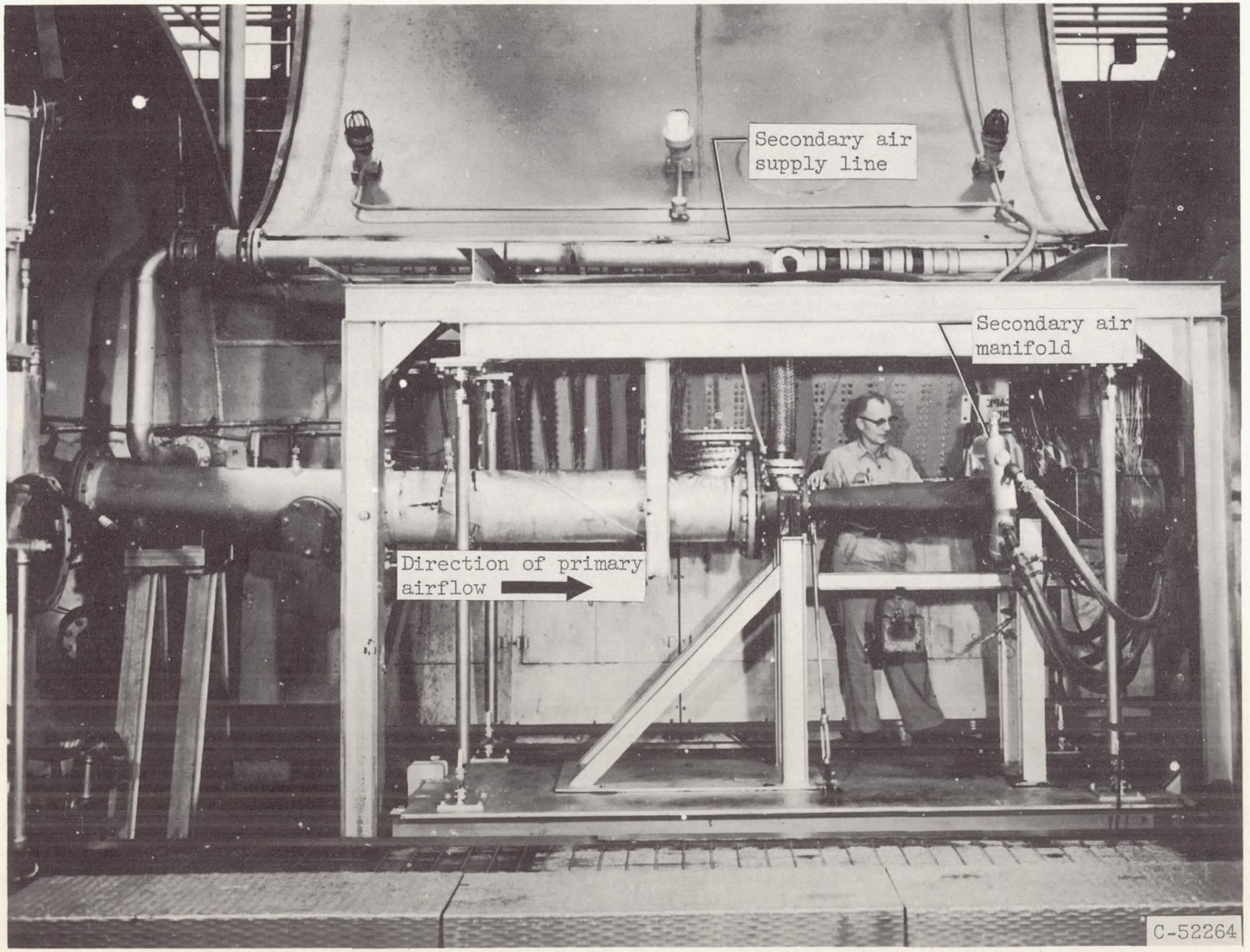

Figure 1. - Nozzle test rig installed in altitude facility.

CONFIDENTIAL

CONFIDENTIAL

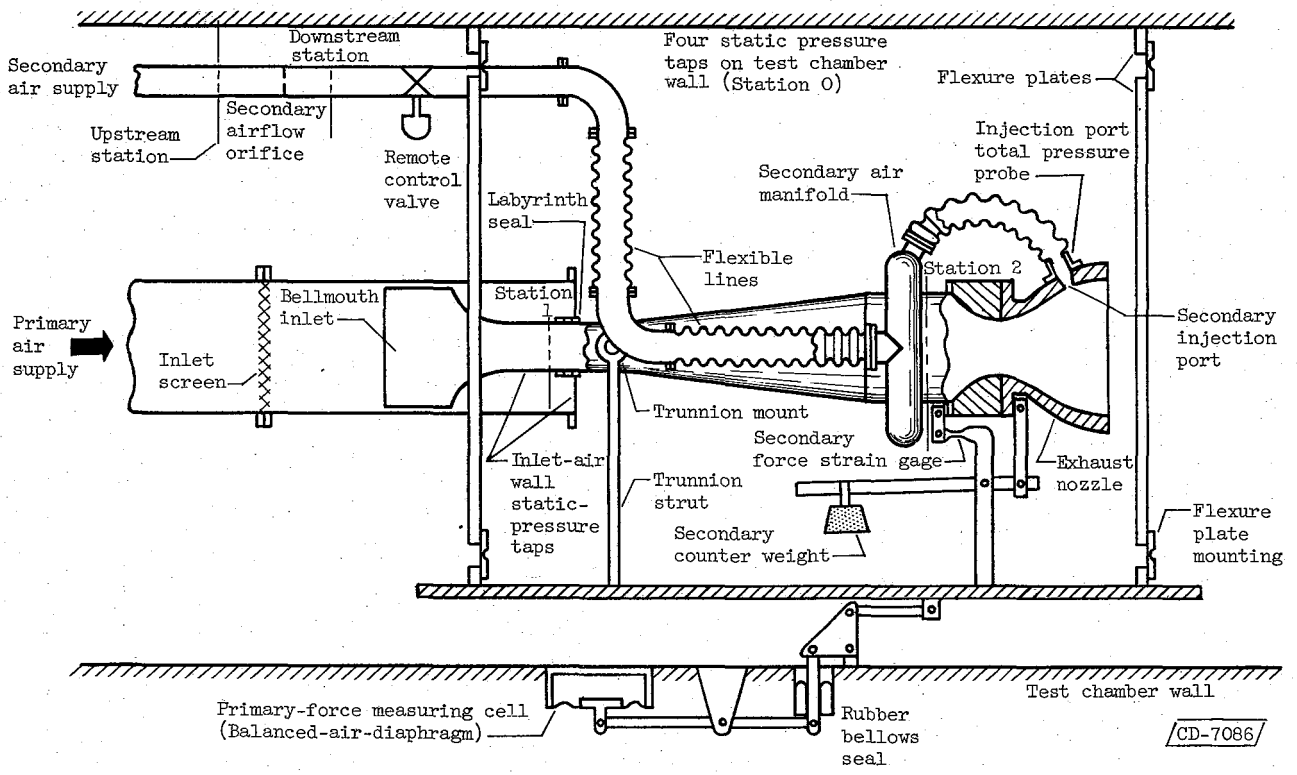

Station		Total-pressure probes	Static-pressure taps	Boundary rakes	Thermocouples
1 (Weight-flow measuring station)		12	10	3	7
2 (Primary-nozzle-inlet station)		20	6	-	-
0 (Ambient)		-	4	-	-
Secondary airflow measuring station	Upstream	-	4	-	3
	Downstream	-	4	-	-
Secondary injection port		5	-	-	-
x (Constant-area inlet duct)		-	5	-	-

Figure 2. - Sketch of nozzle rig showing instrumentation locations.

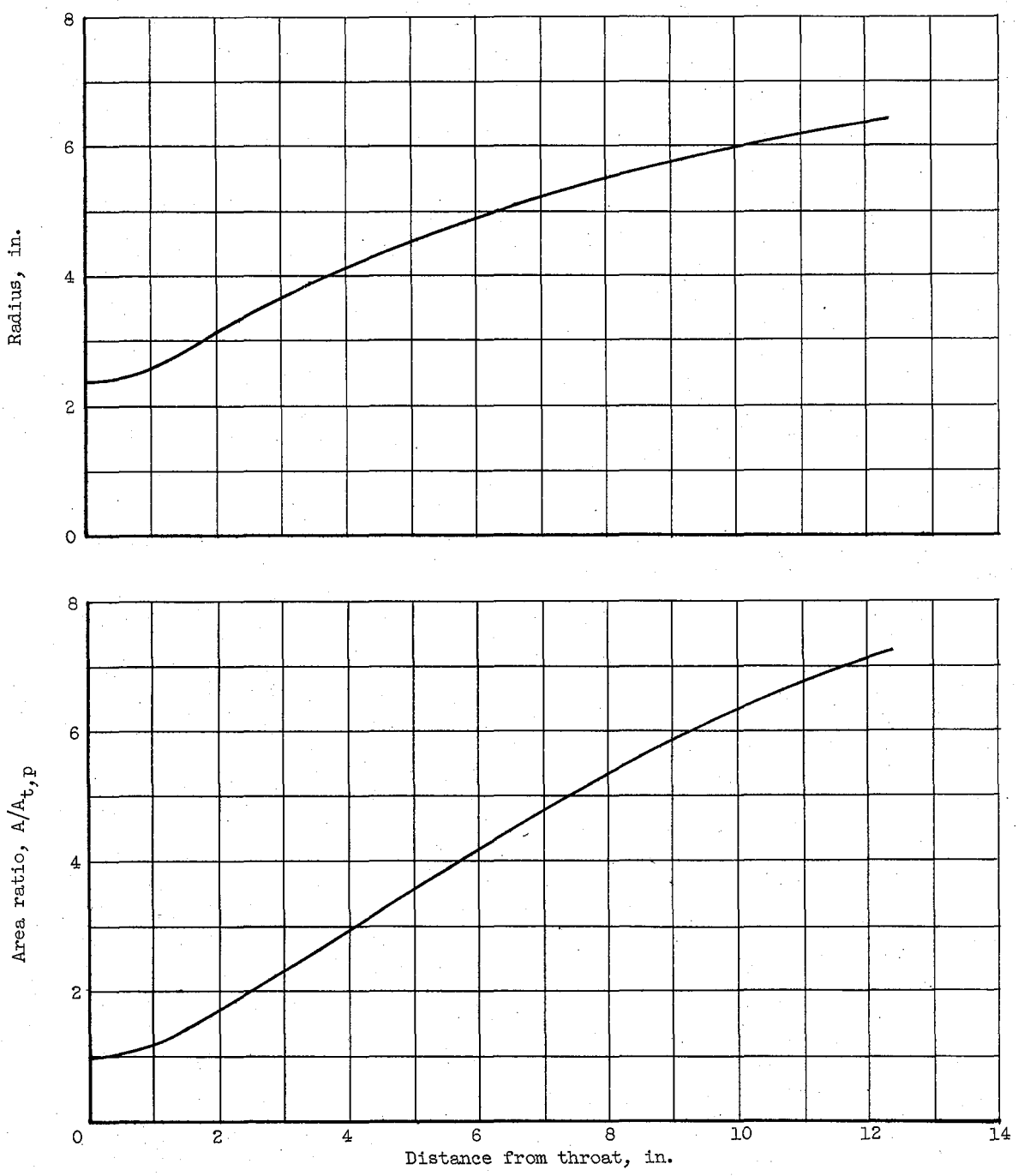

Figure 3. - Coordinates and variation of flow area for primary bell nozzle.

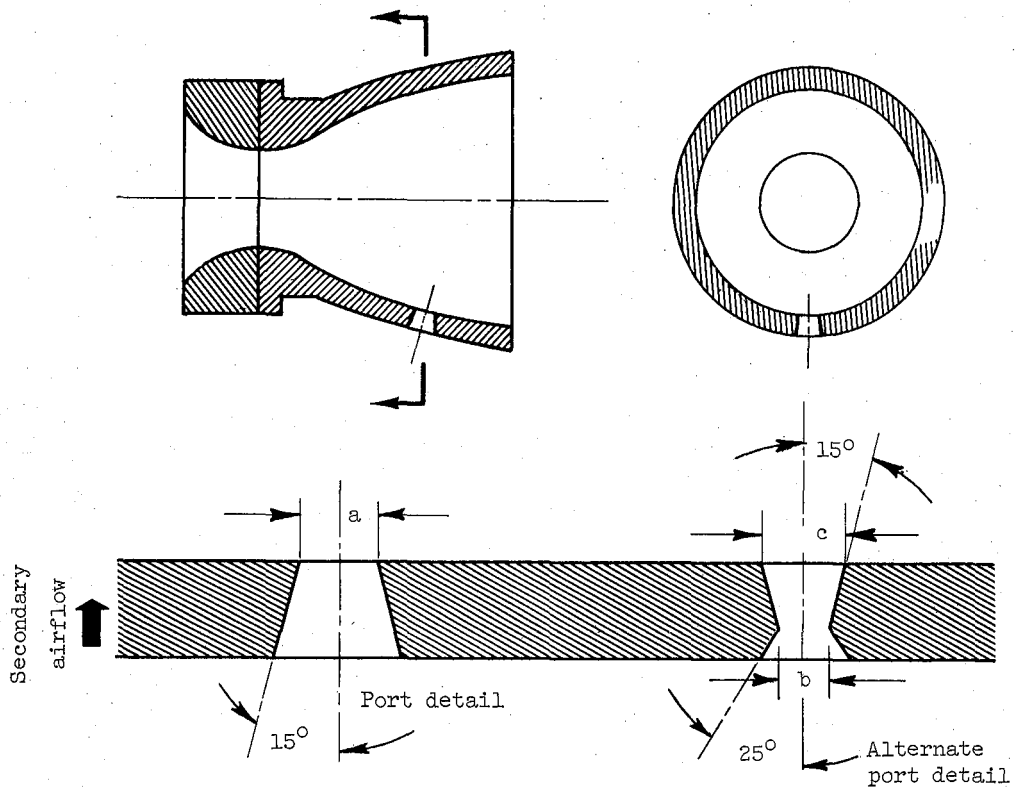

Configuration	Axial location of port, $A/A_{t,p}$	a, in.	b, in.	c, in.	Secondary-port-exit Mach number
Large single radial injection; axial position 1	4.72	1.18	----	----	1.00
Large single radial injection; axial position 2	5.98	1.18	----	----	1.00
Large single radial injection; axial position 3	6.97	1.18	----	----	1.00
Small single radial injection; axial position 2	5.98	.97	----	----	1.00
Small single radial injection; axial position 3	6.97	.97	----	----	1.00
Single radial convergent-divergent injection; expansion ratio, 3.4	5.98	----	1.02	1.89	2.78
Single radial convergent-divergent injection; expansion ratio, 5.7	5.98	----	.80	1.91	3.31

(a) Schematic description.

Figure 4. - Single radial injection configurations.

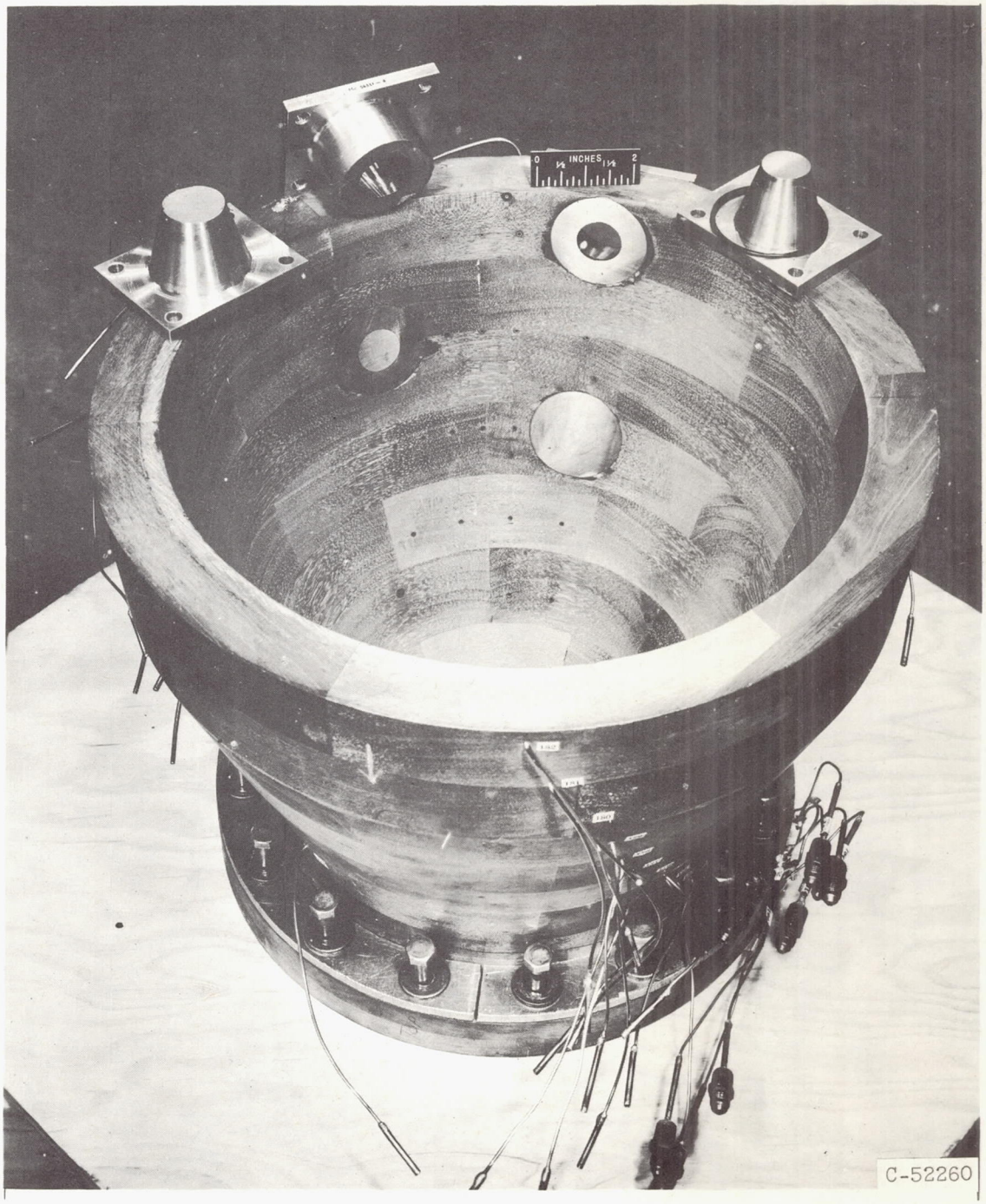

(b) Three-quarter view of test hardware.

Figure 4. - Concluded. Single radial injection configurations.

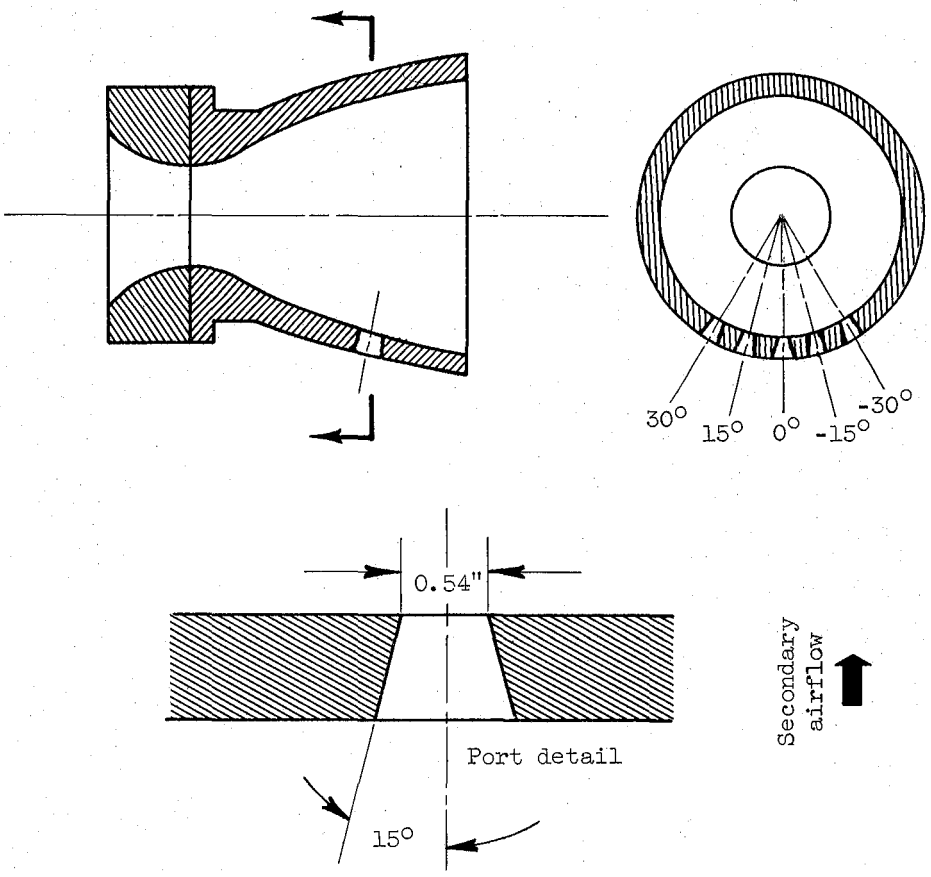

Configuration	Number of ports	Axial location of port, $A/A_{t,p}$	Circumferential location
Multiple radial injection; axial position 1	5	4.72	30°,15°,0°,-15°,-30°
Multiple radial injection; axial position 2	5	5.98	30°,15°,0°,-15°,-30°
Multiple radial injection; axial position 3	5	6.97	30°,15°,0°,-15°,-30°
Multiple radial injection; axial position 2	3	5.98	30°,0°,-30°
Axial multiple radial injection	3	4.72 5.98 6.97	0°

(a) Schematic description.

Figure 5. - Multiple radial injection configurations.

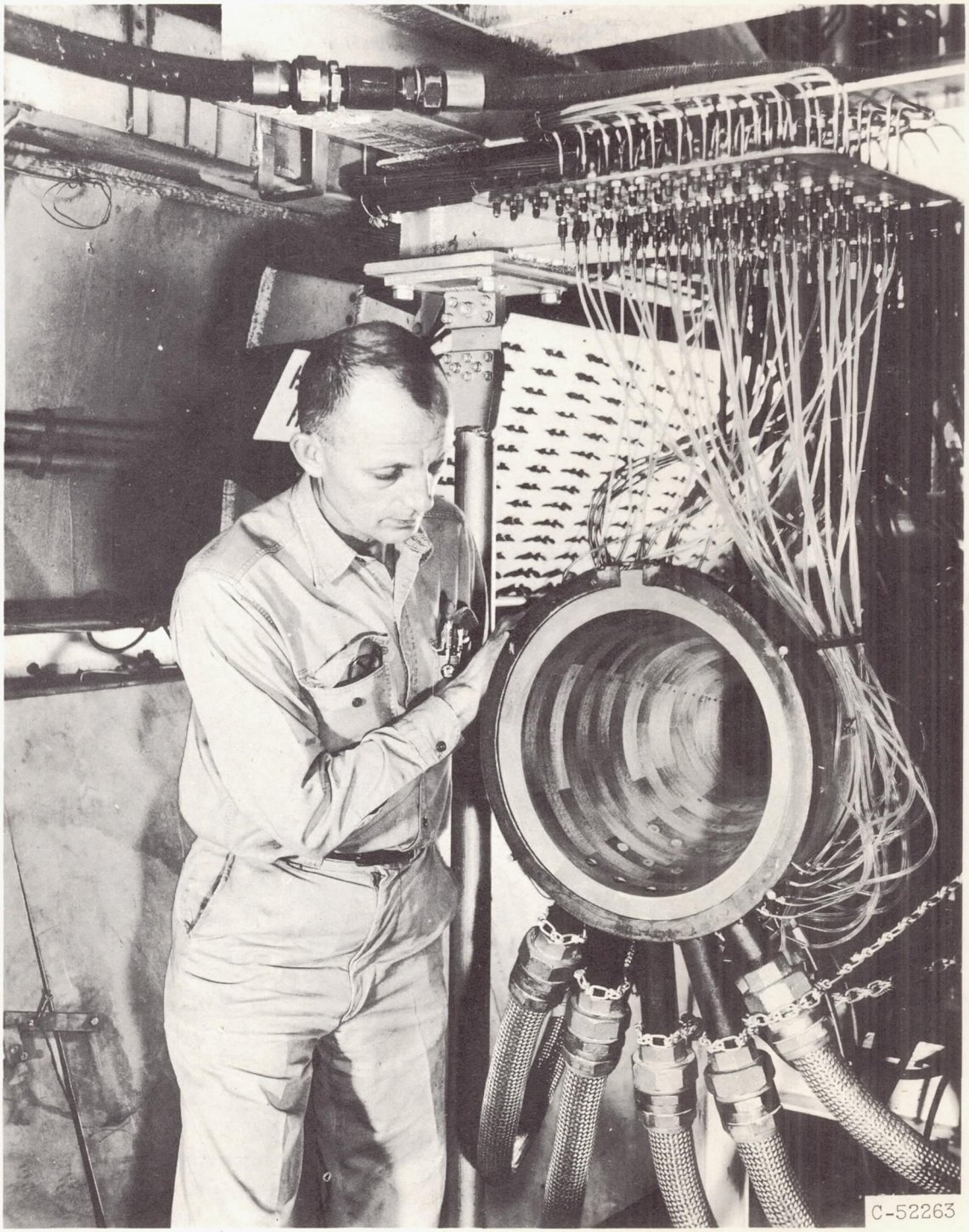

(b) Three-quarter view of test hardware.

Figure 5. - Concluded. Multiple radial injection configurations.

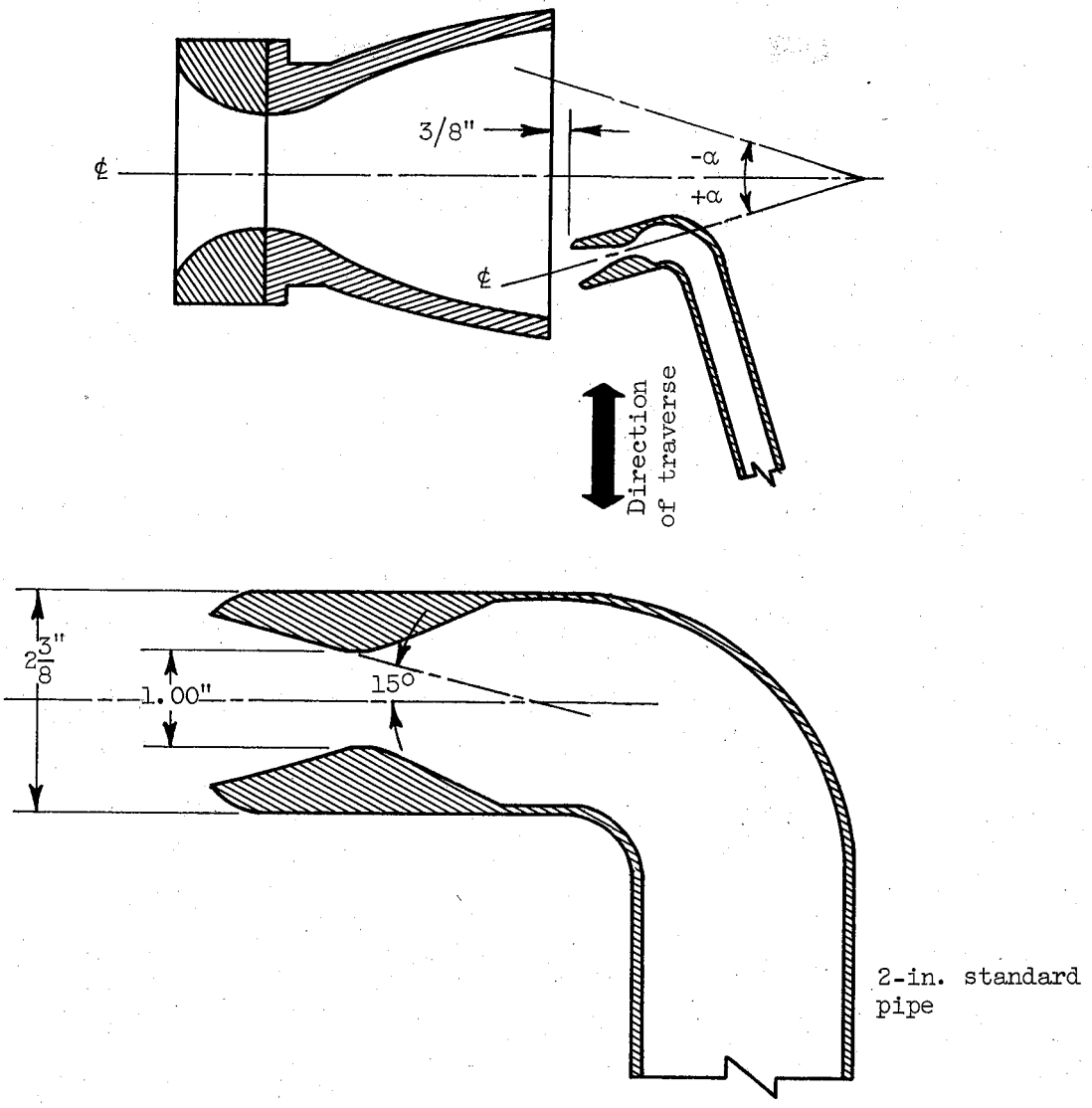

Counterstream-nozzle expansion ratio	Counterstream flow angle, α, deg	Counterstream-nozzle-exit Mach number
2.9	0	2.6
2.2	0	2.3
1.7	0	2.0
2.2	-10	2.3
2.2	10	2.3
2.2	20	2.3

Figure 6. - Low-pressure counterstream injection configurations.

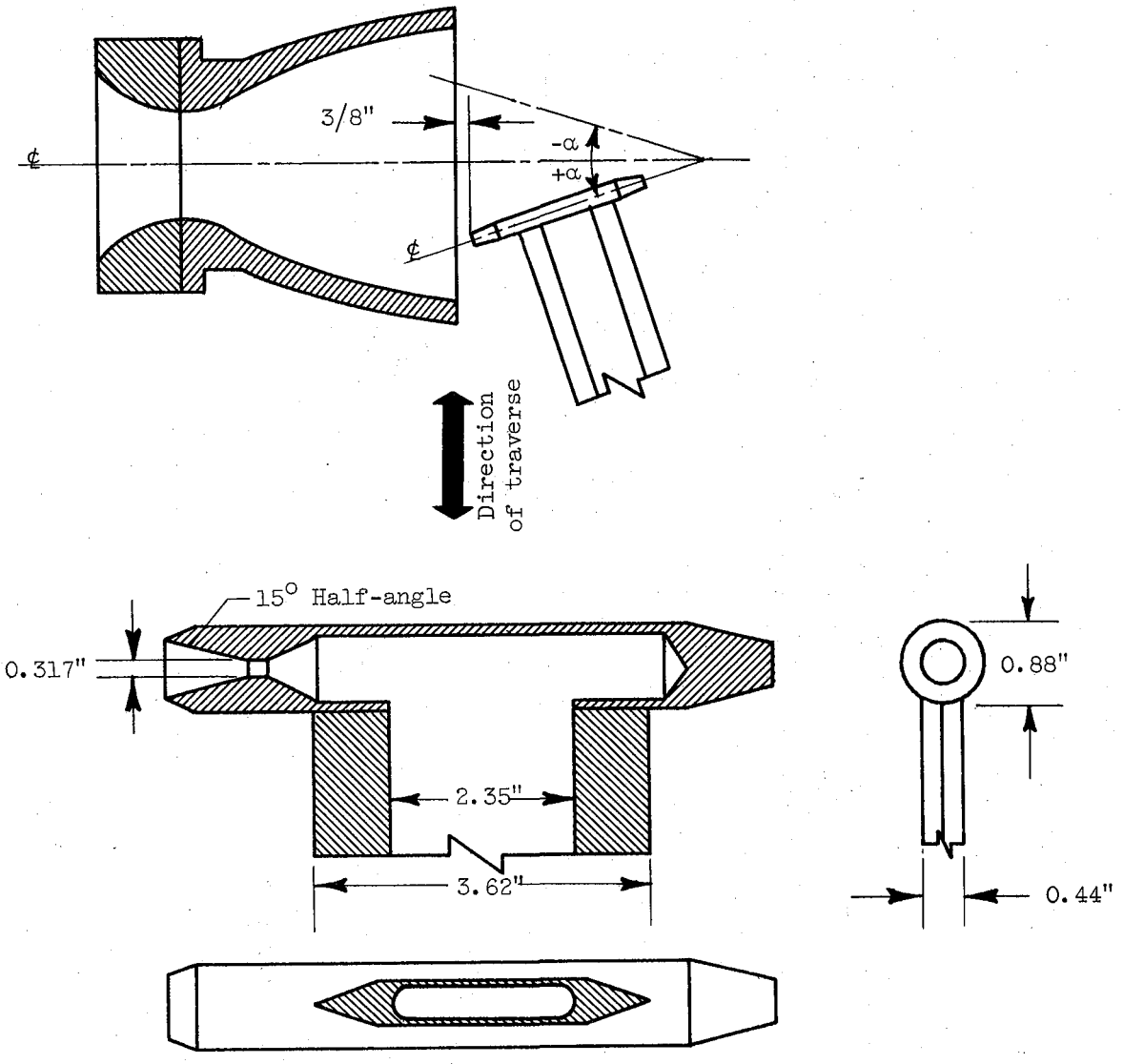

Counterstream-nozzle expansion ratio	Counterstream flow angle, α, deg	Counterstream-nozzle-exit Mach number
6.5	0	3.5
3.6	0	2.8
2.0	0	2.2
6.5	10	3.5
3.6	10	2.8
2.0	10	2.2
2.0	20	2.2

(a) Schematic description.

Figure 7. - High-pressure counterstream injection configurations.

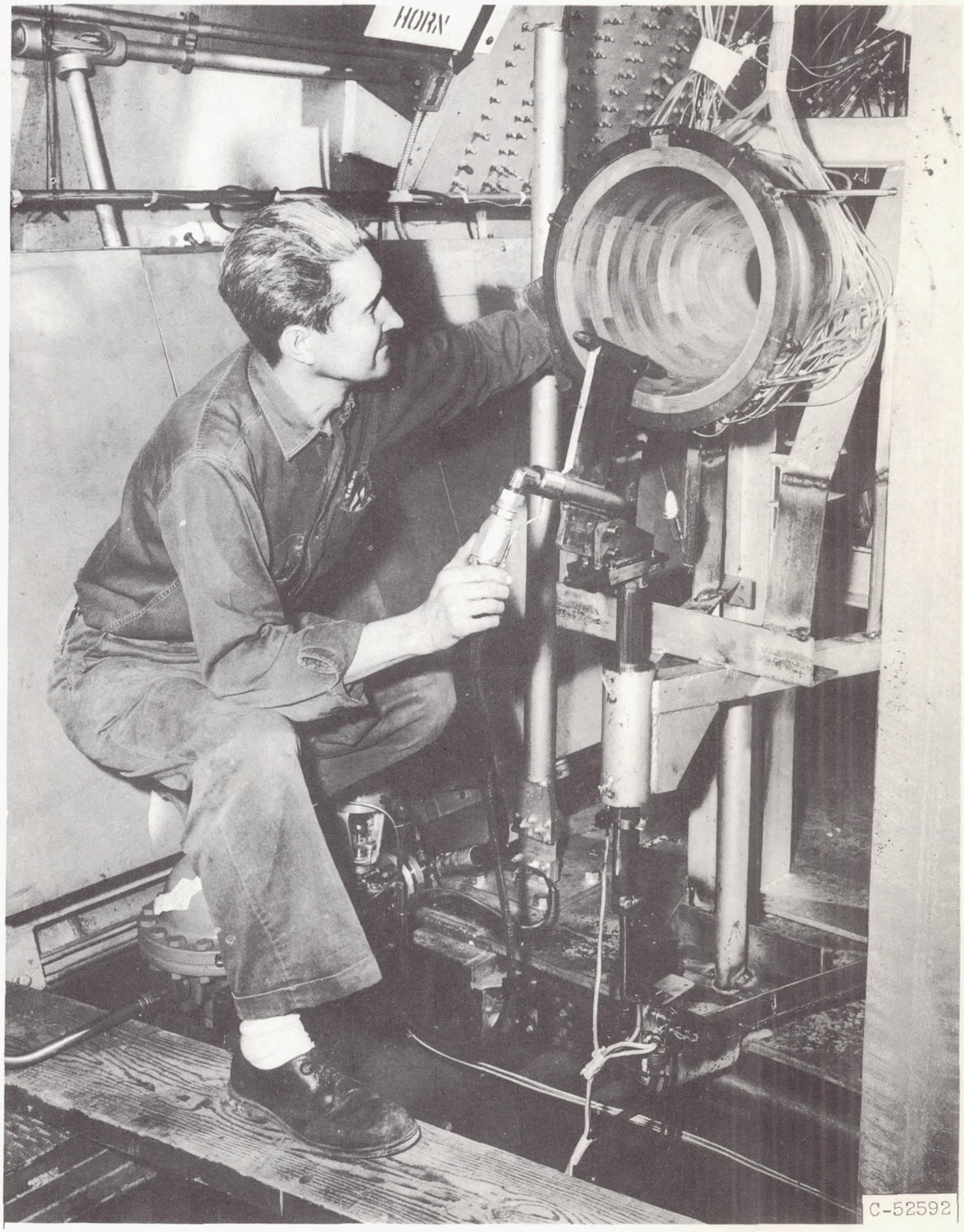

(b) Three-quarter view of test hardware.

Figure 7. - Concluded. High-pressure counterstream injection configurations.

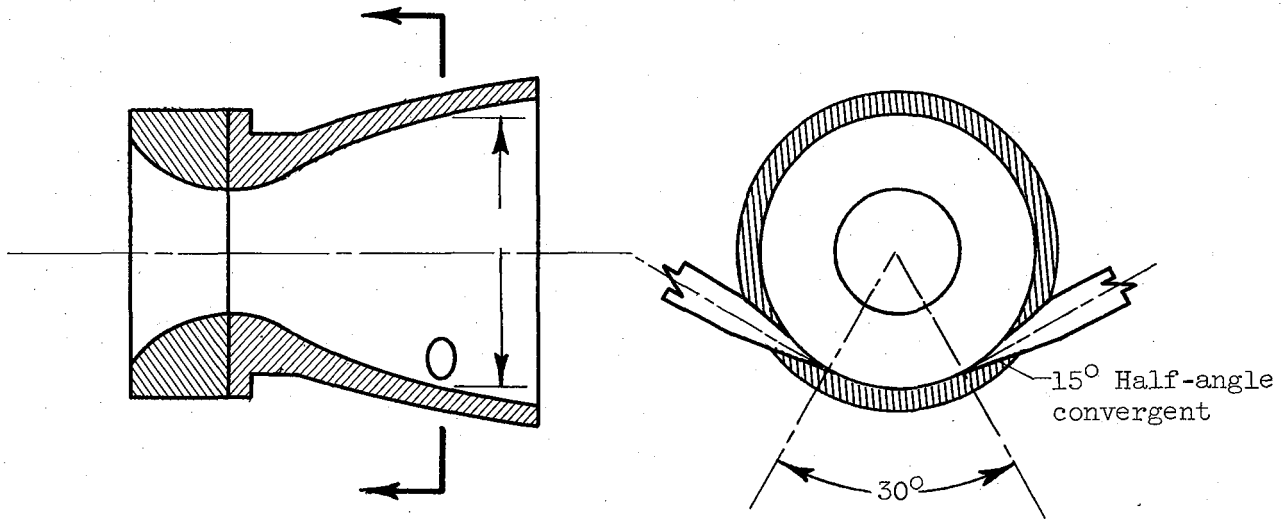

	Axial location of port, $A/A_{t,p}$
Axial position 1	4.72
Axial position 2	5.98
Axial position 3	6.97

Figure 8. - Tangential injection configurations. Minimum diameter on tangential injection port, 0.83 inch.

CONFIDENTIAL

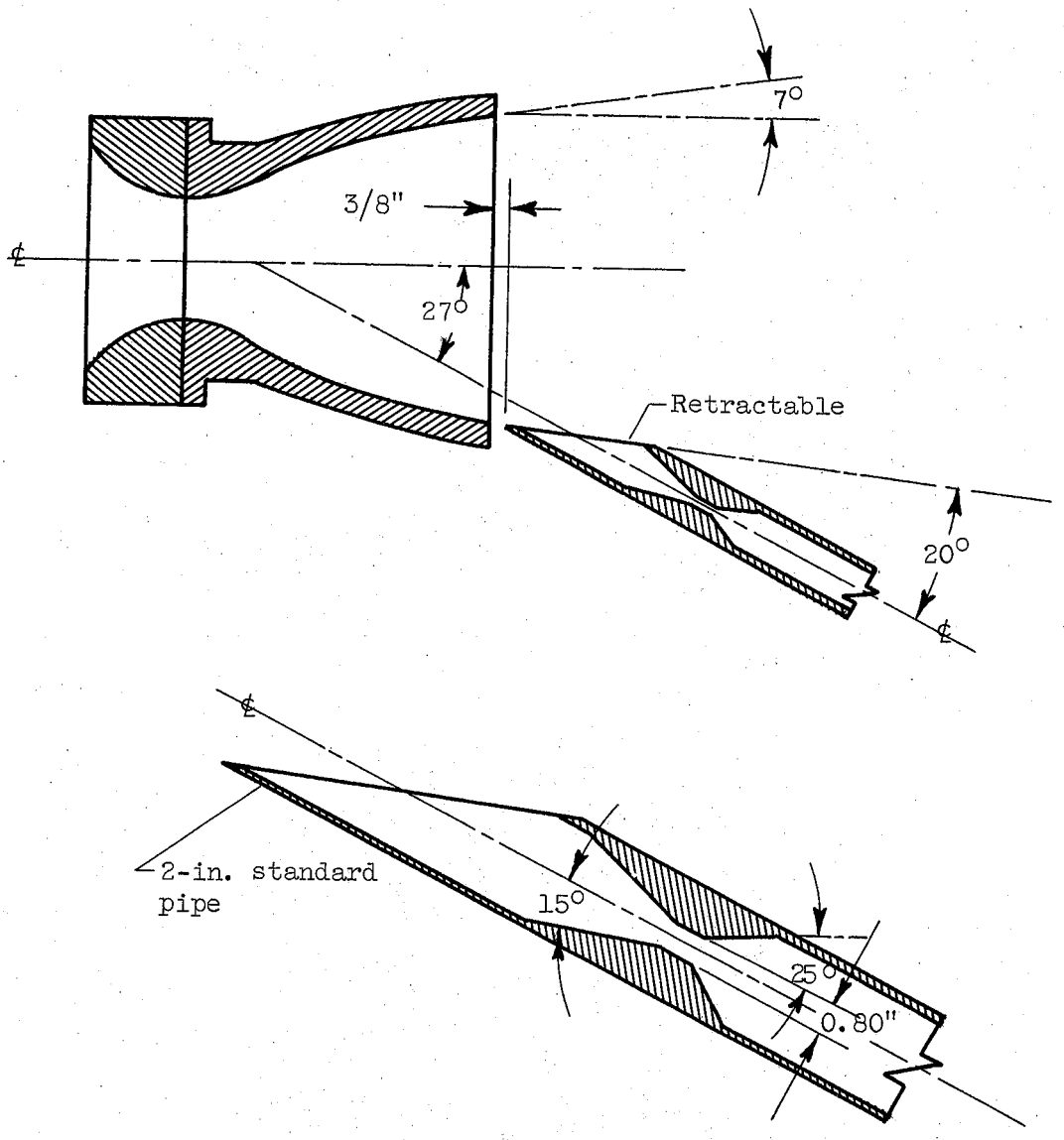

Figure 9. - Slanted-tube injection configuration.

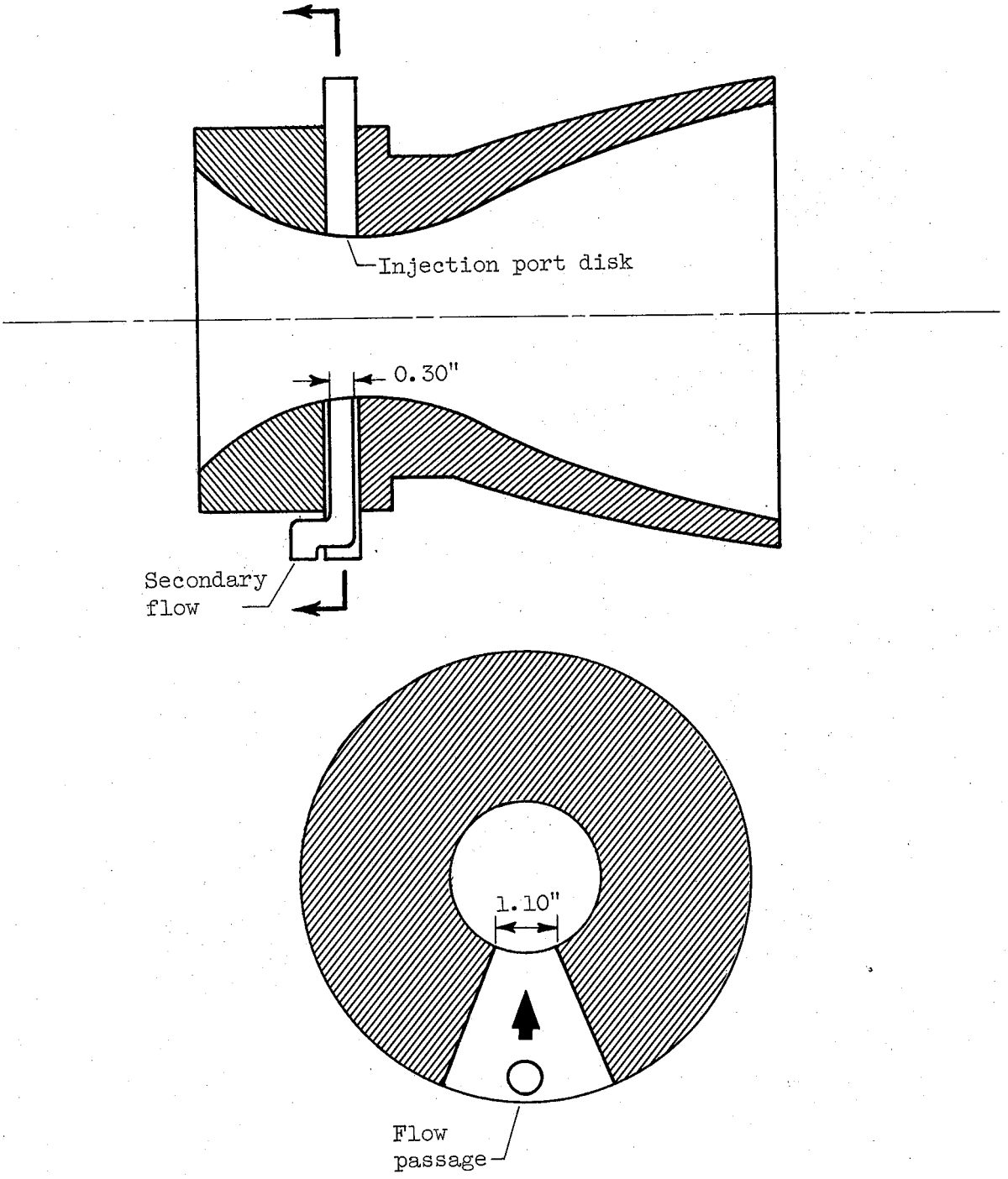

Figure 10. - Throat injection configuration.

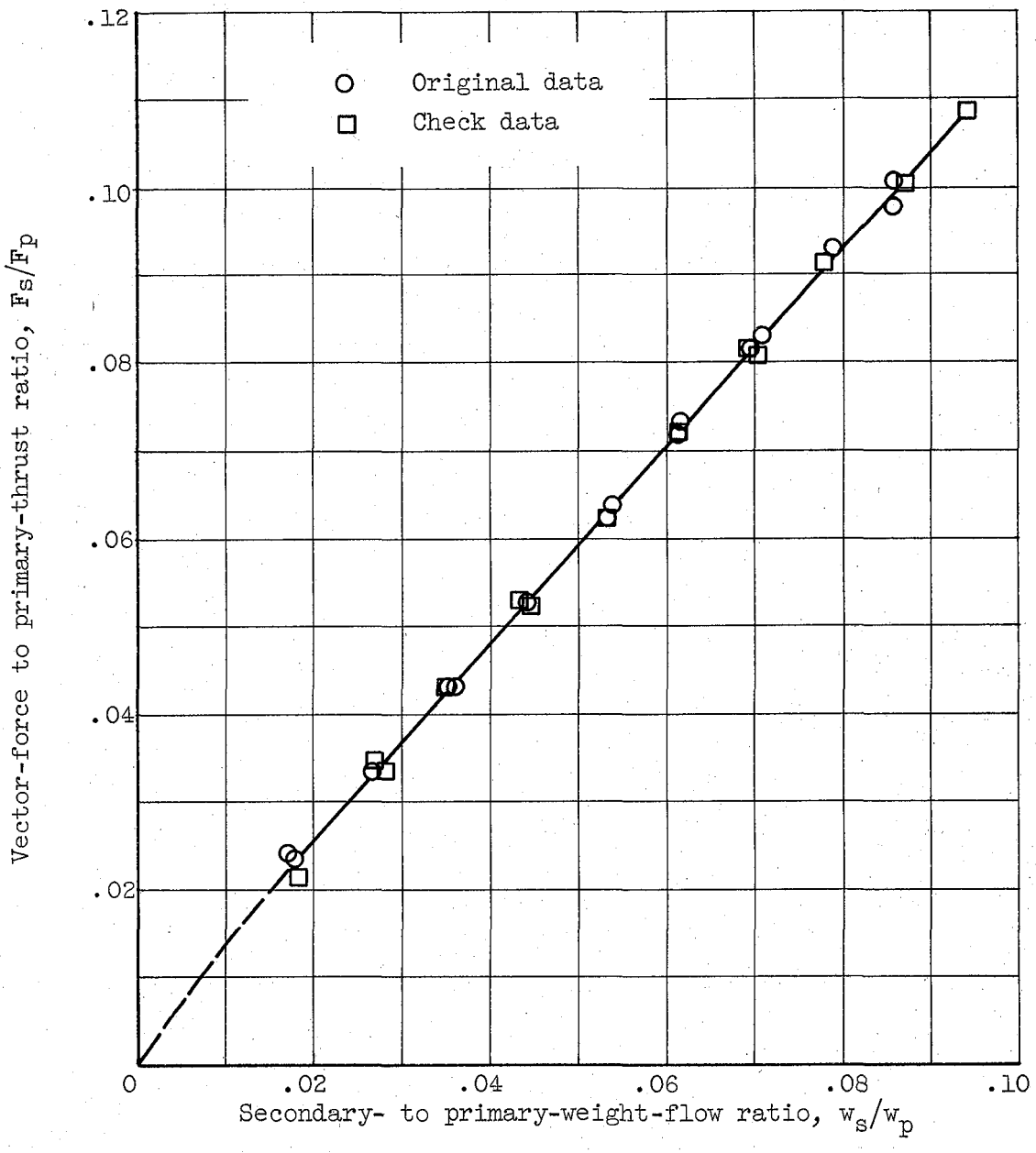

Figure 11. - Check on data reproducibility.

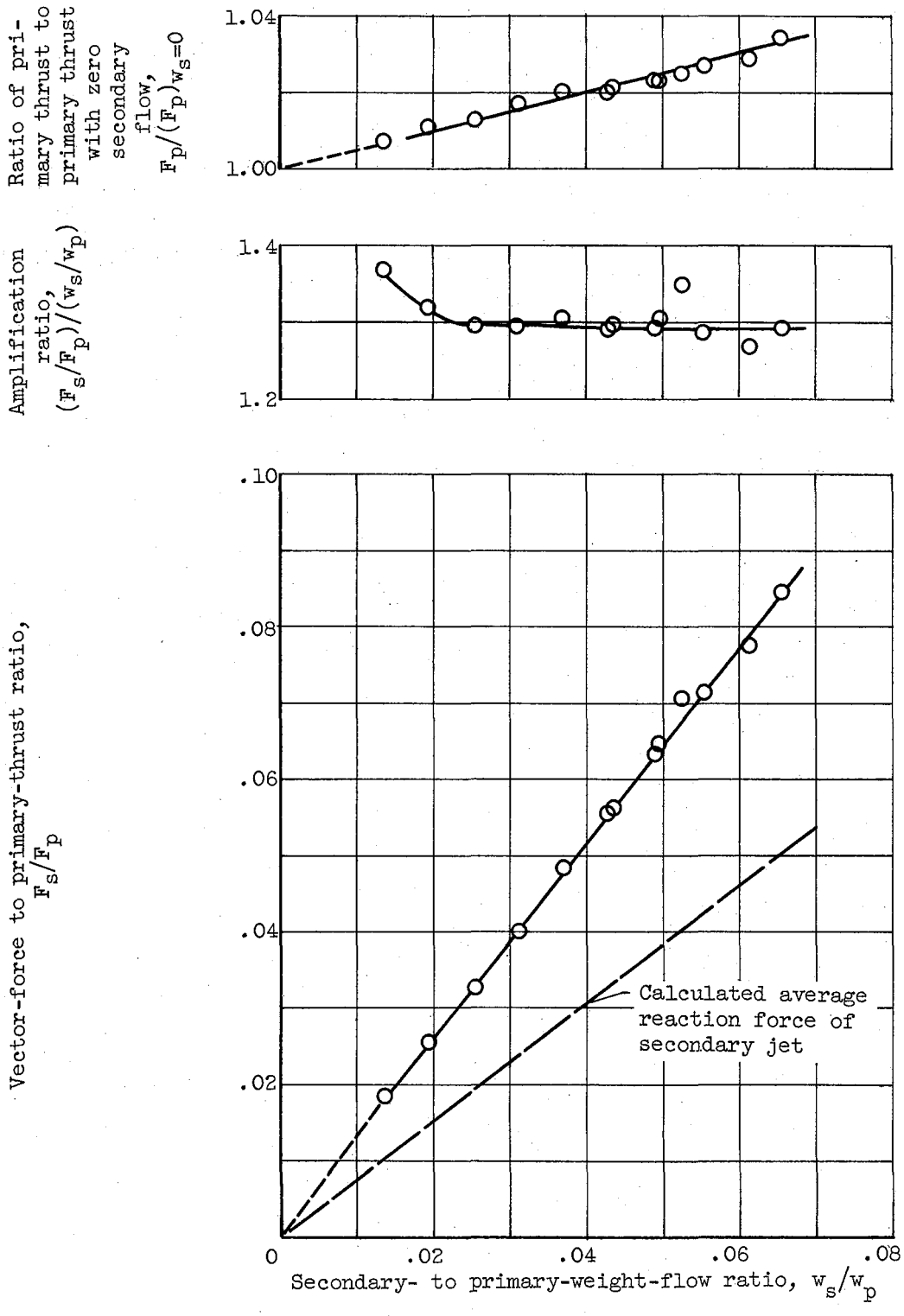

Figure 12. - Typical performance for radial injection configurations.

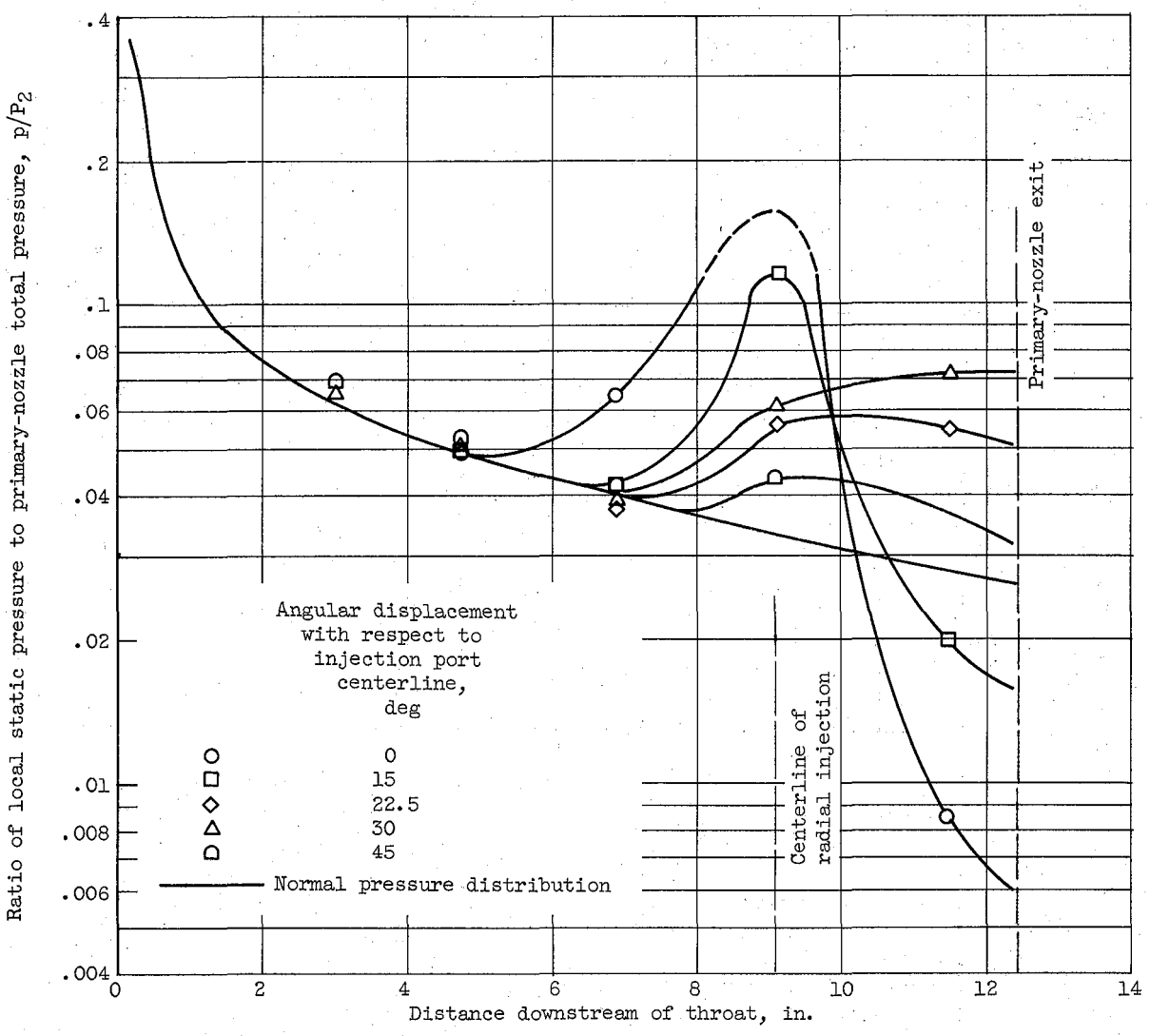

Figure 13. - Typical primary-nozzle static-pressure distribution for radial injection configurations.

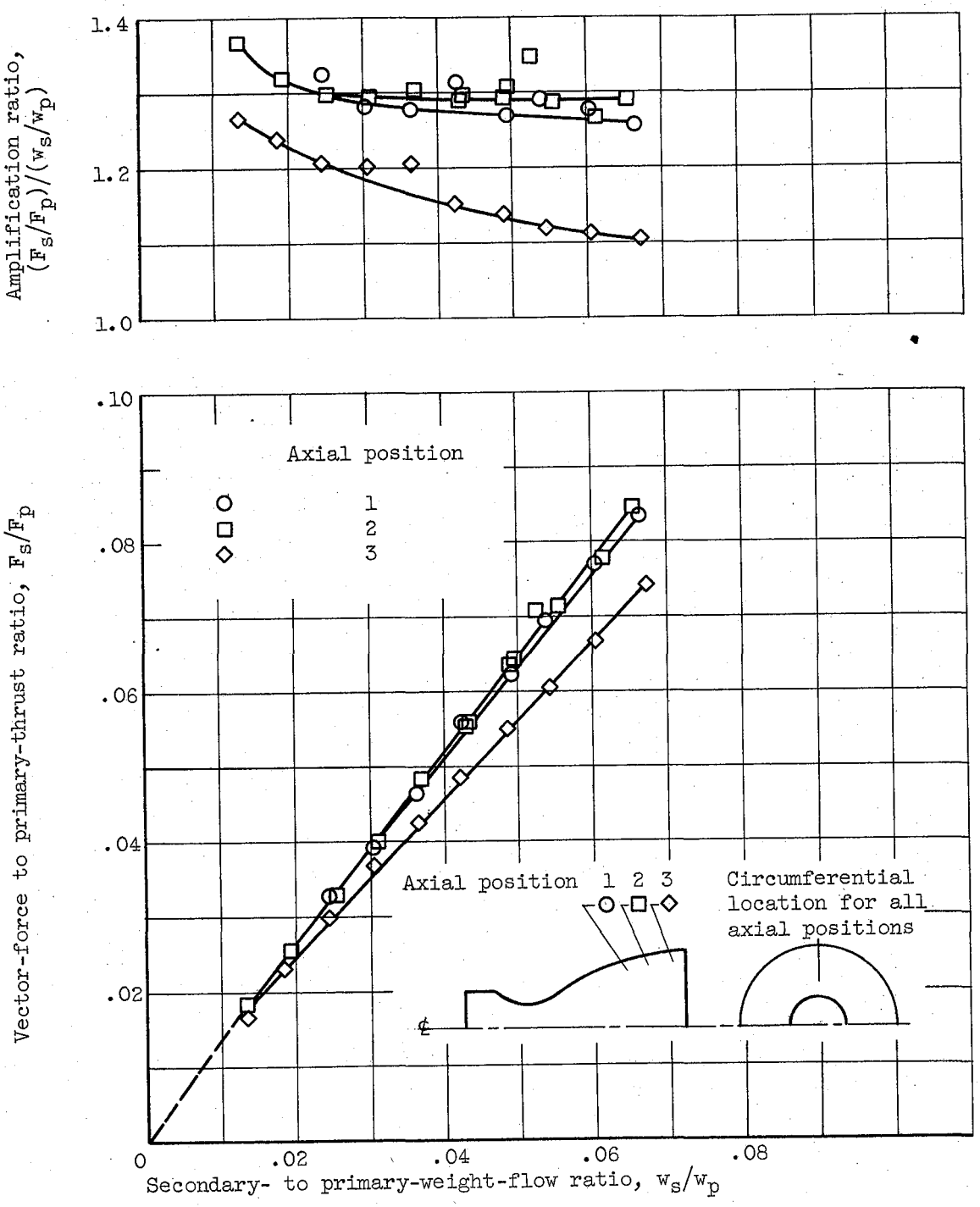

(a) Single large port.

Figure 14. - Effect of secondary-port axial location on performance of radial injection configurations.

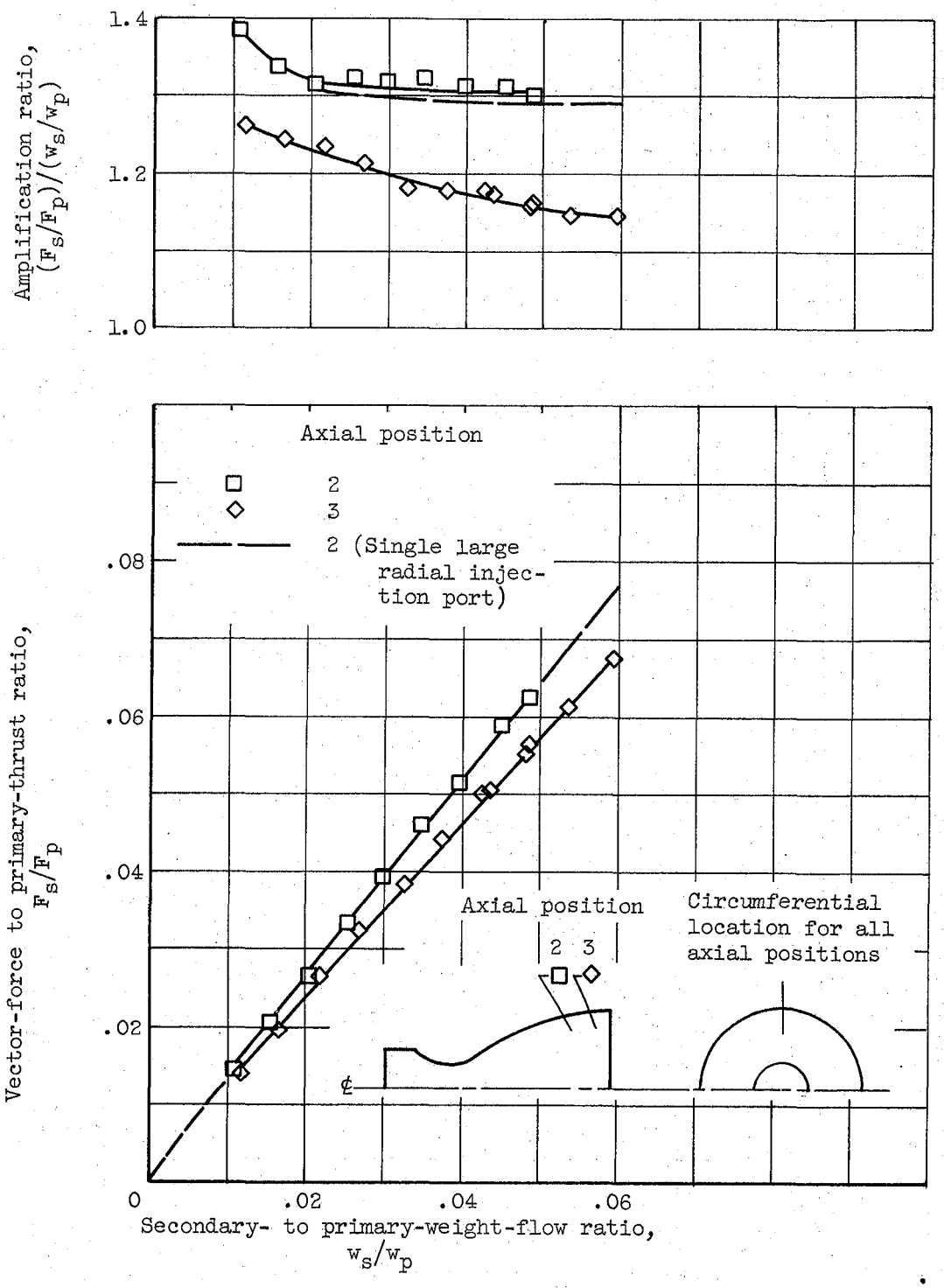

(b) Single small port.

Figure 14. - Continued. Effect of secondary-port axial location on performance of radial injection configurations.

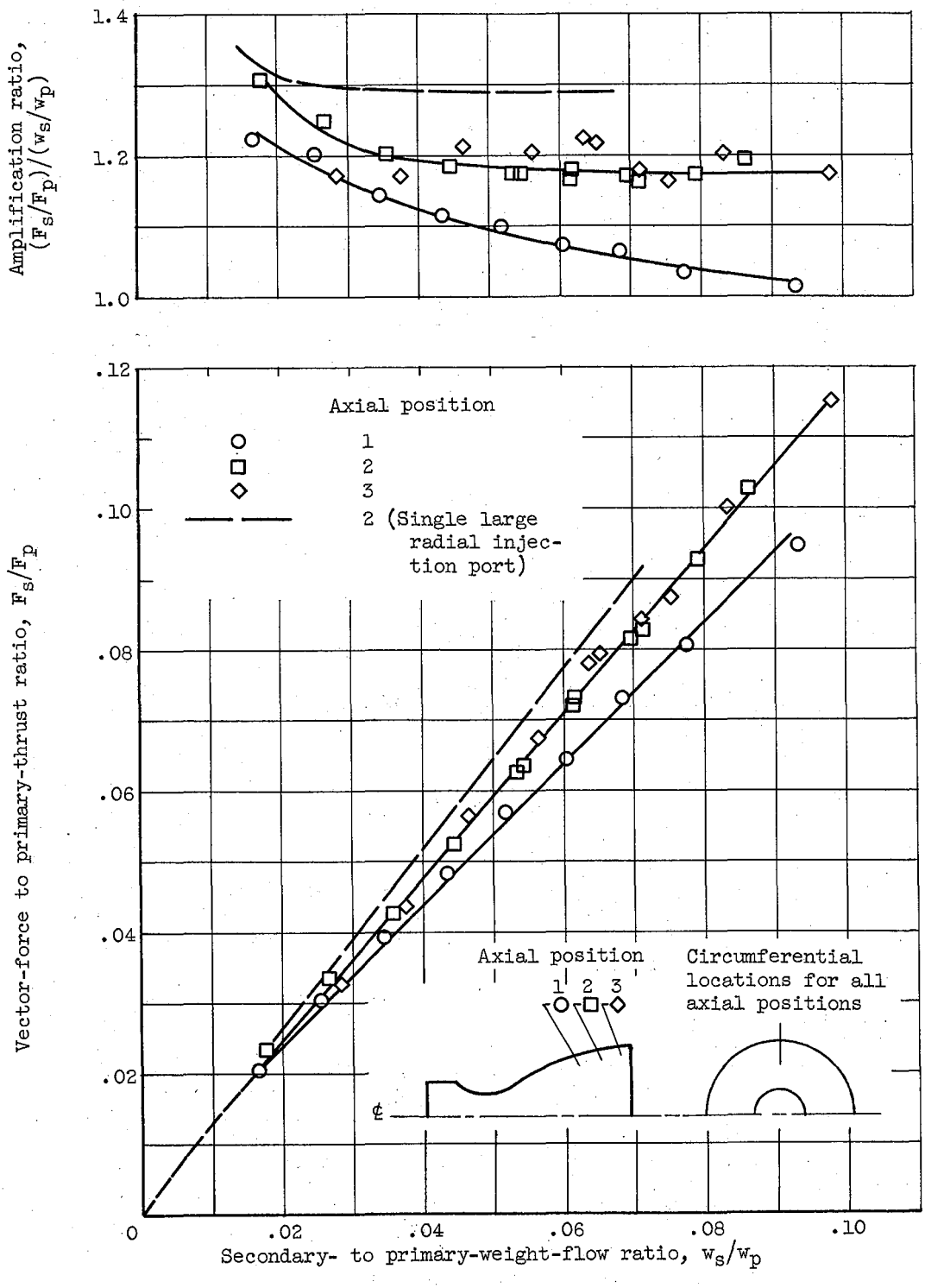

(c) Multiple ports.

Figure 14. - Concluded. Effect of secondary-port axial location on performance of radial injection configurations.

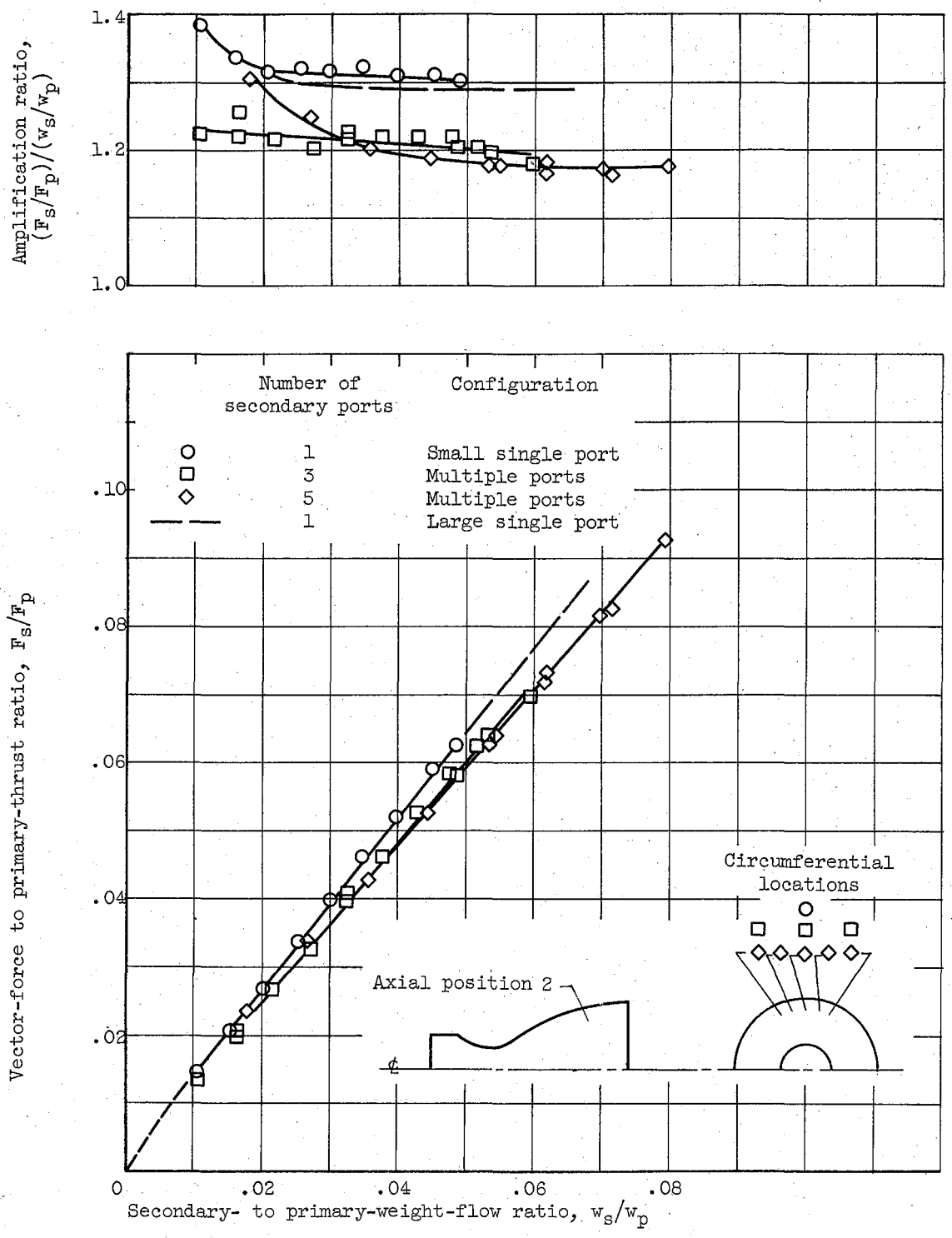

Figure 15. - Effect of number of secondary radial injection ports. Axial position 2.

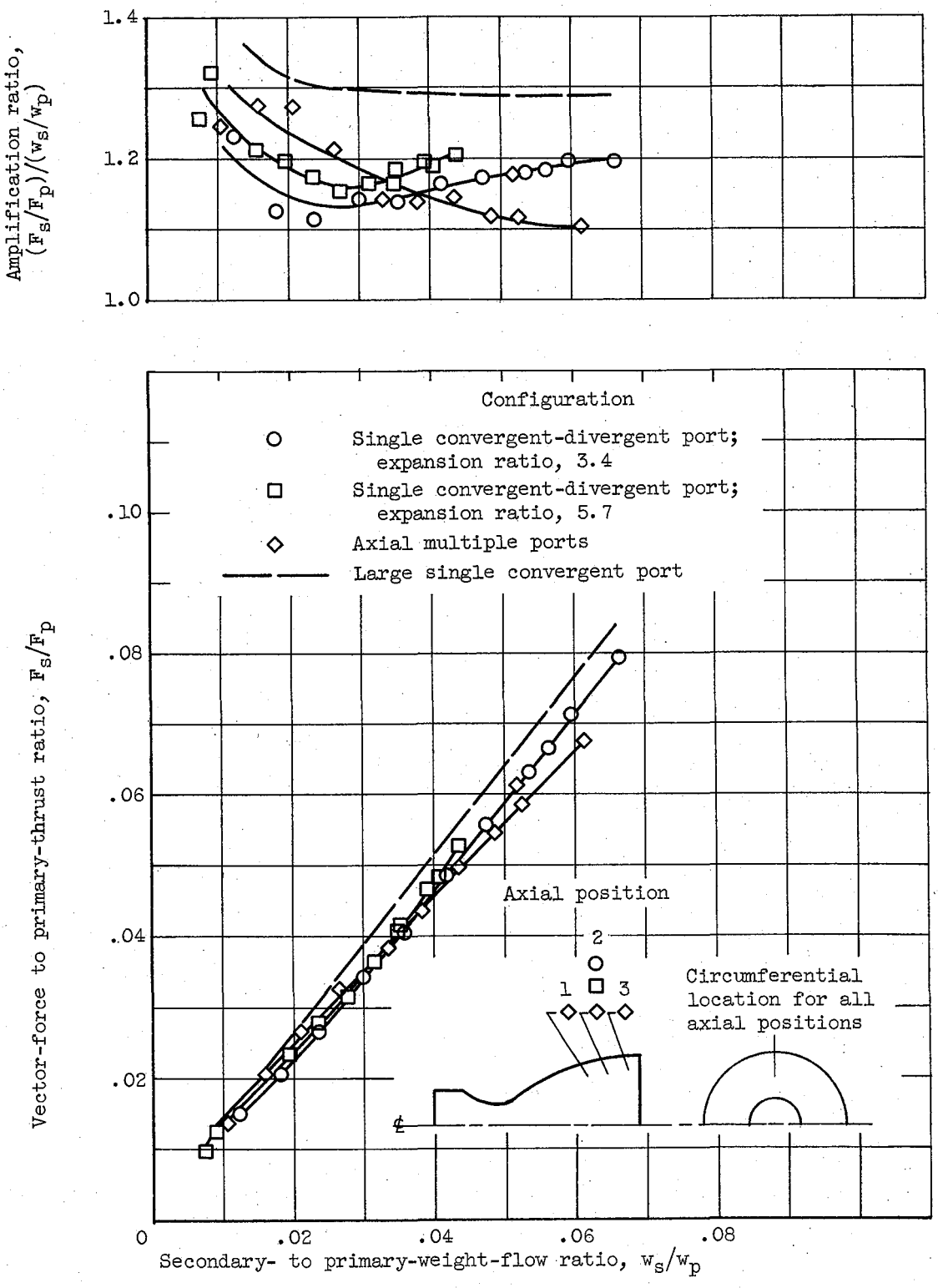

Figure 16. - Performance of axial multiple and single convergent-divergent ports.

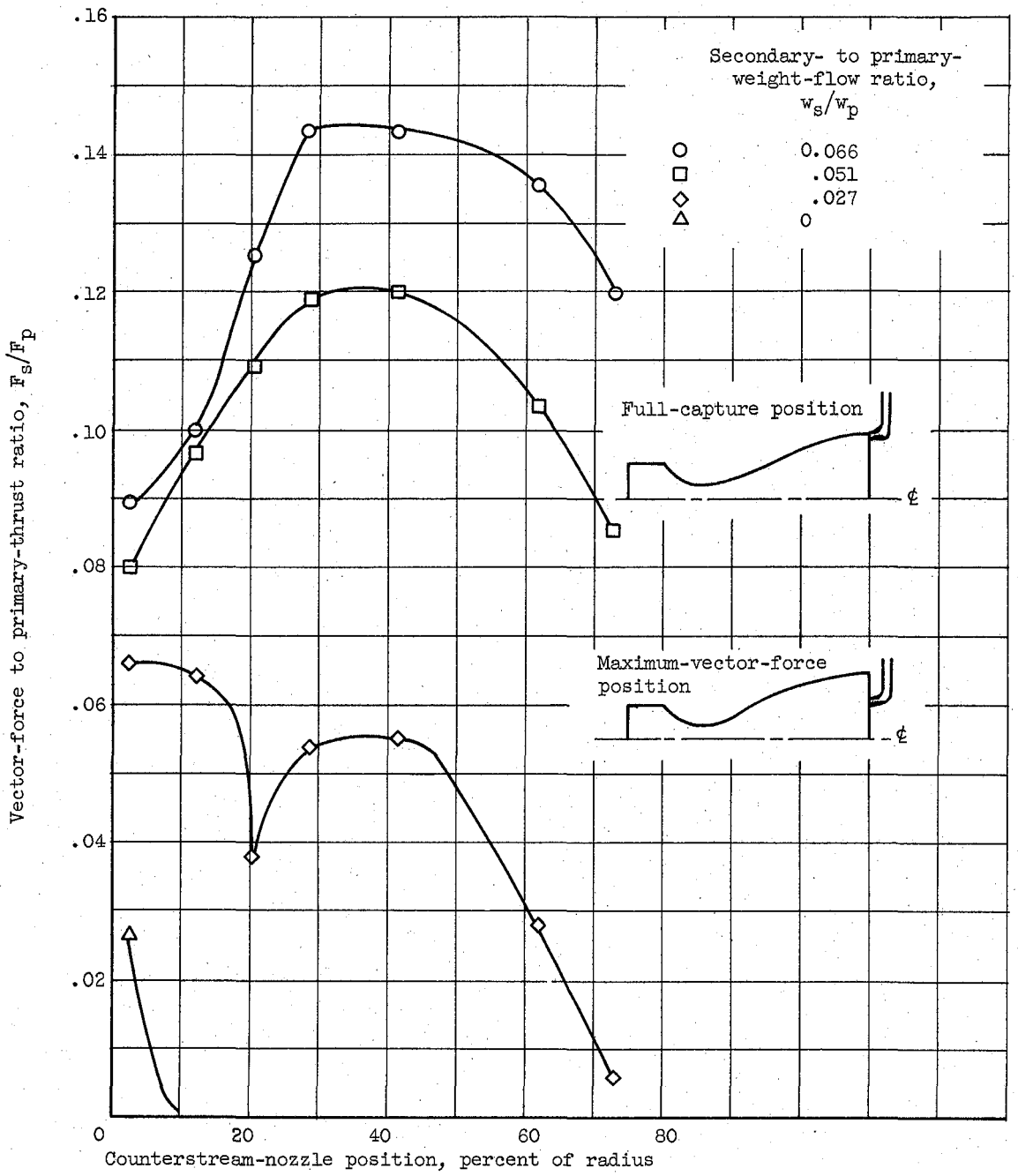

Figure 17. - Typical effect of low-pressure counterstream-nozzle position on vector force.

Figure 18. - Typical performance of low-pressure counterstream injection configuration.

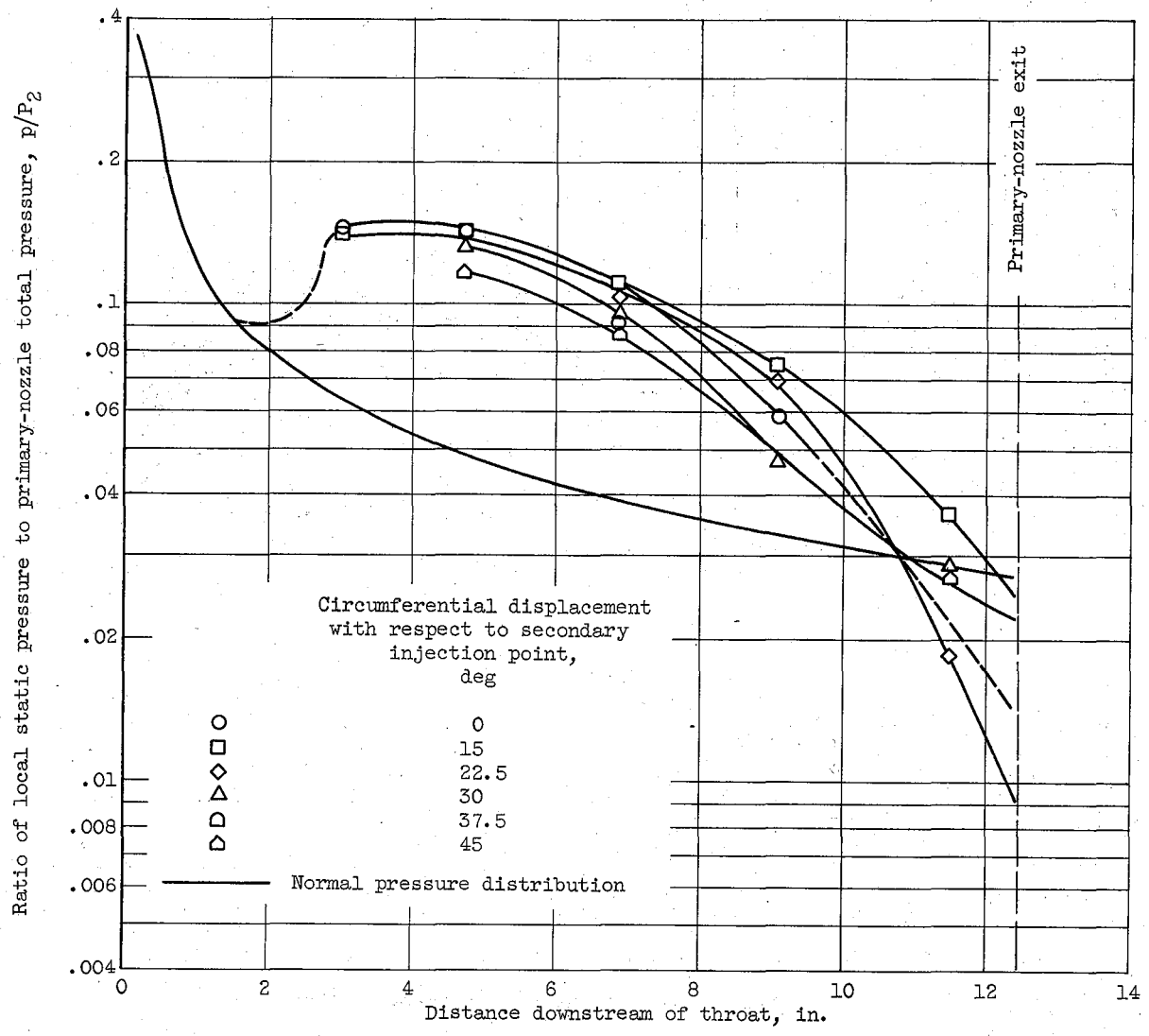

(a) Counterstream nozzle at full-capture position.

Figure 19. - Typical primary-nozzle static-pressure distribution for low-pressure counterstream configurations.

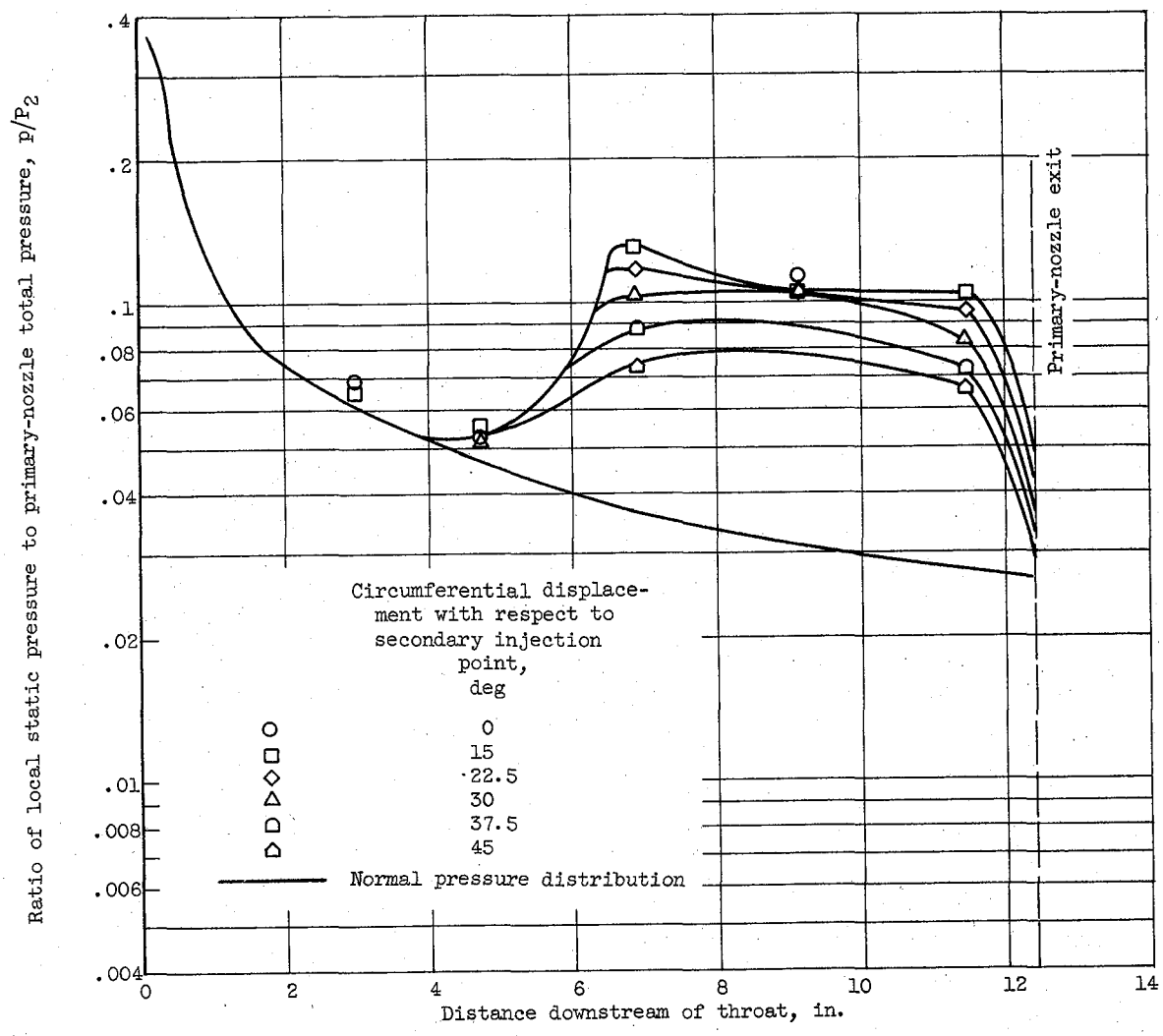

(b) Counterstream nozzle at maximum-vector-force position.

Figure 19. - Concluded. Typical primary-nozzle static-pressure distribution for low-pressure counterstream configurations.

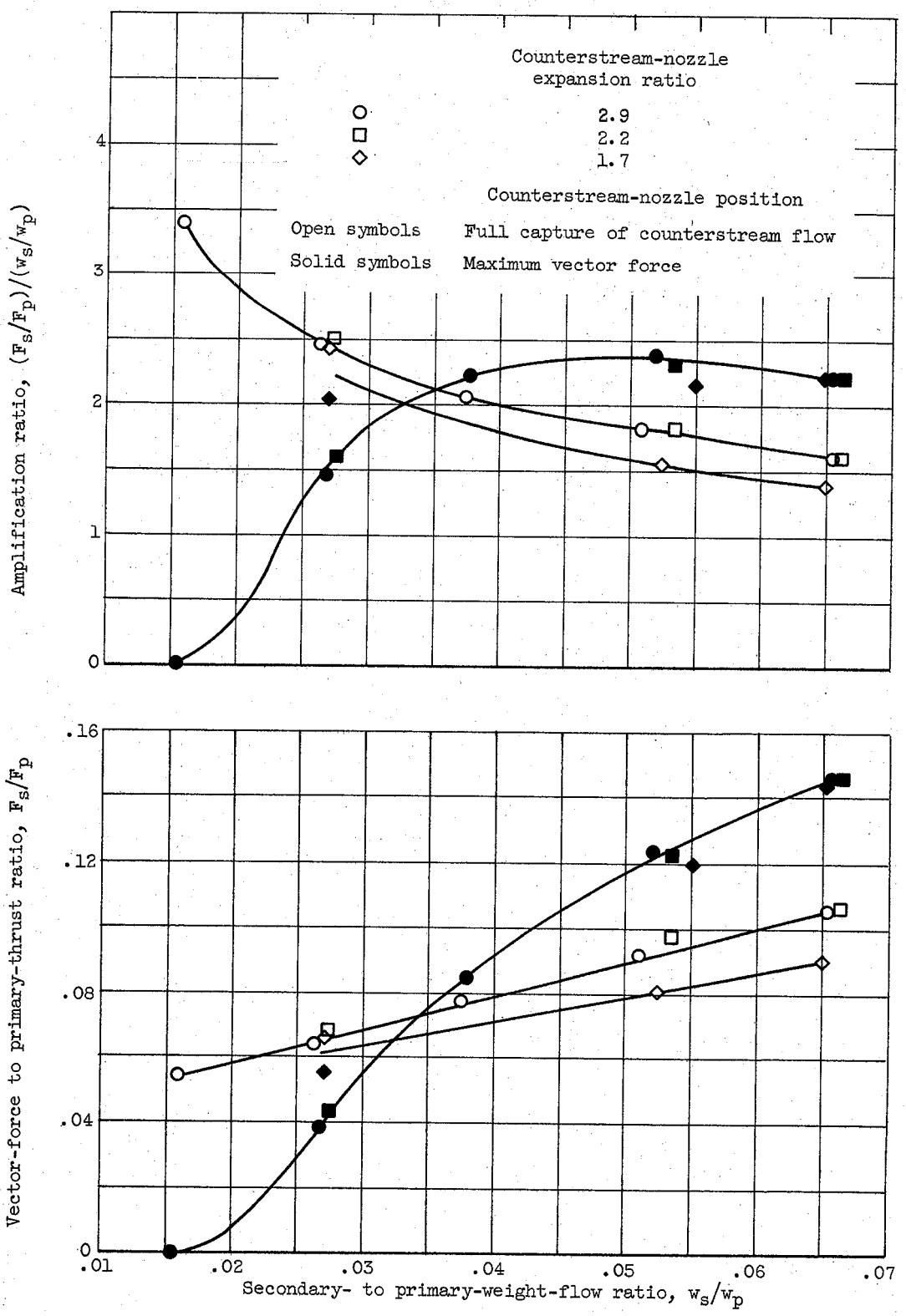

Figure 20. - Effect of counterstream-nozzle expansion ratio.

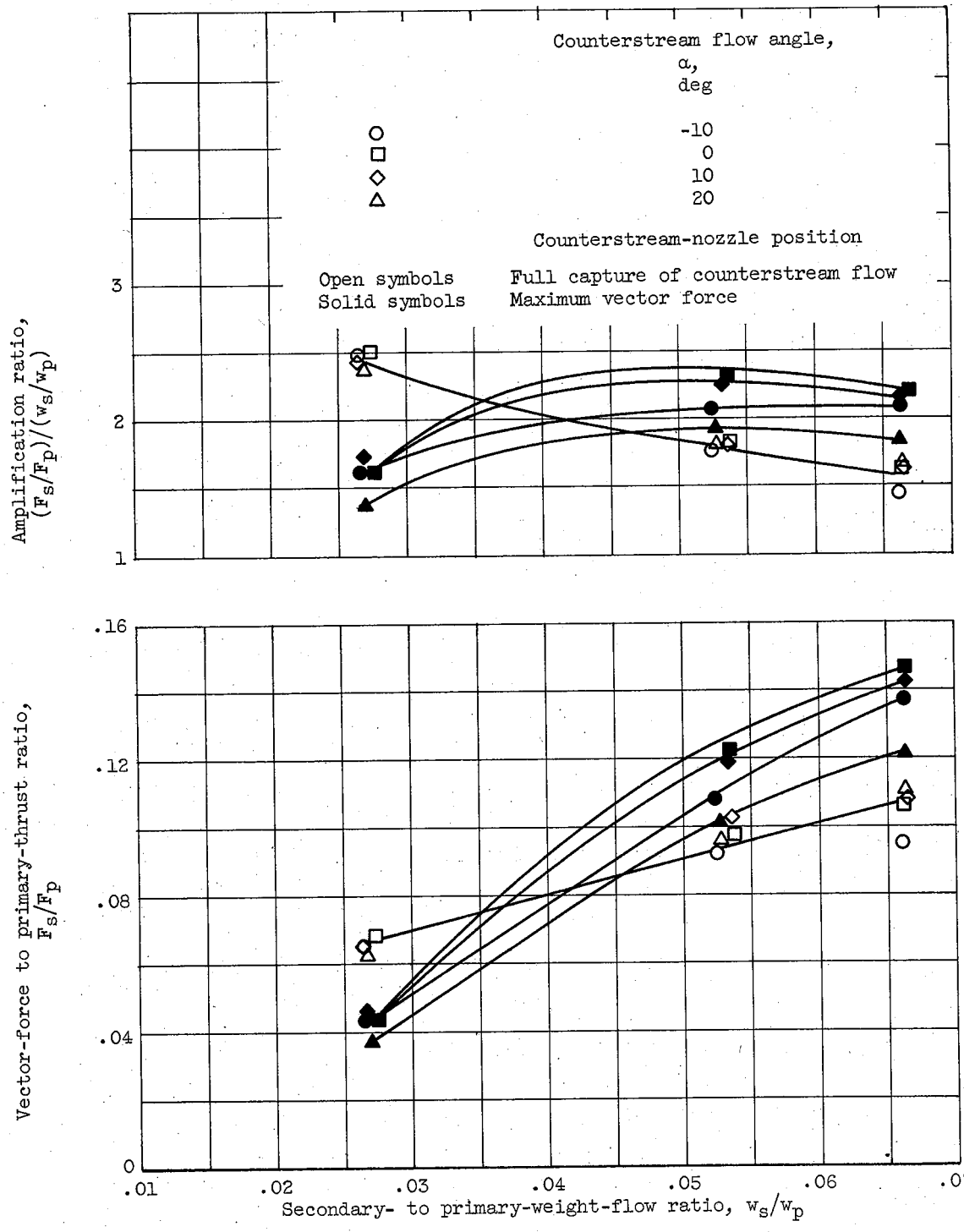

Figure 21. - Effect of counterstream flow angle.

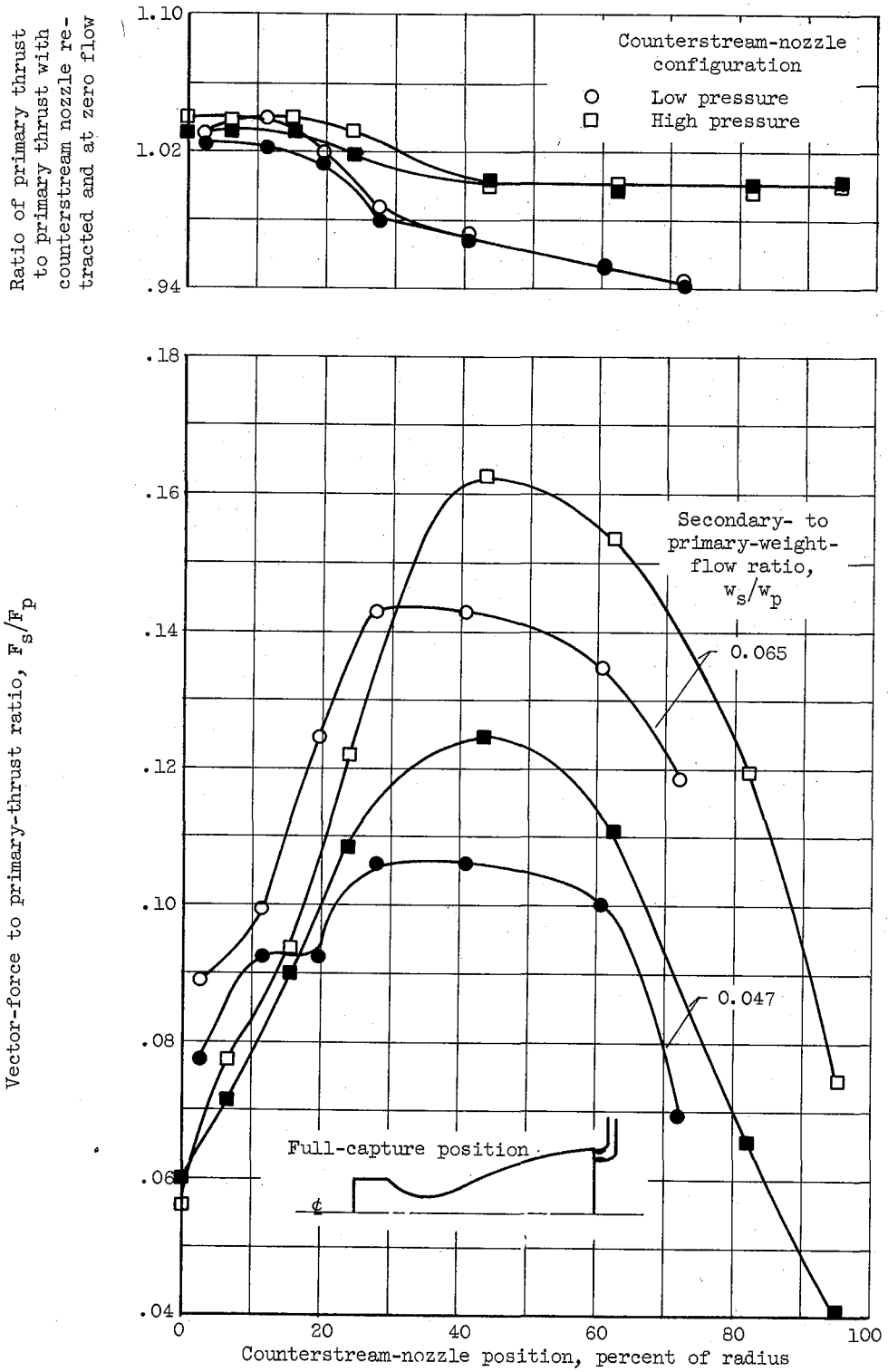

Figure 22. - Performance comparison of low- and high-pressure counterstream configurations.

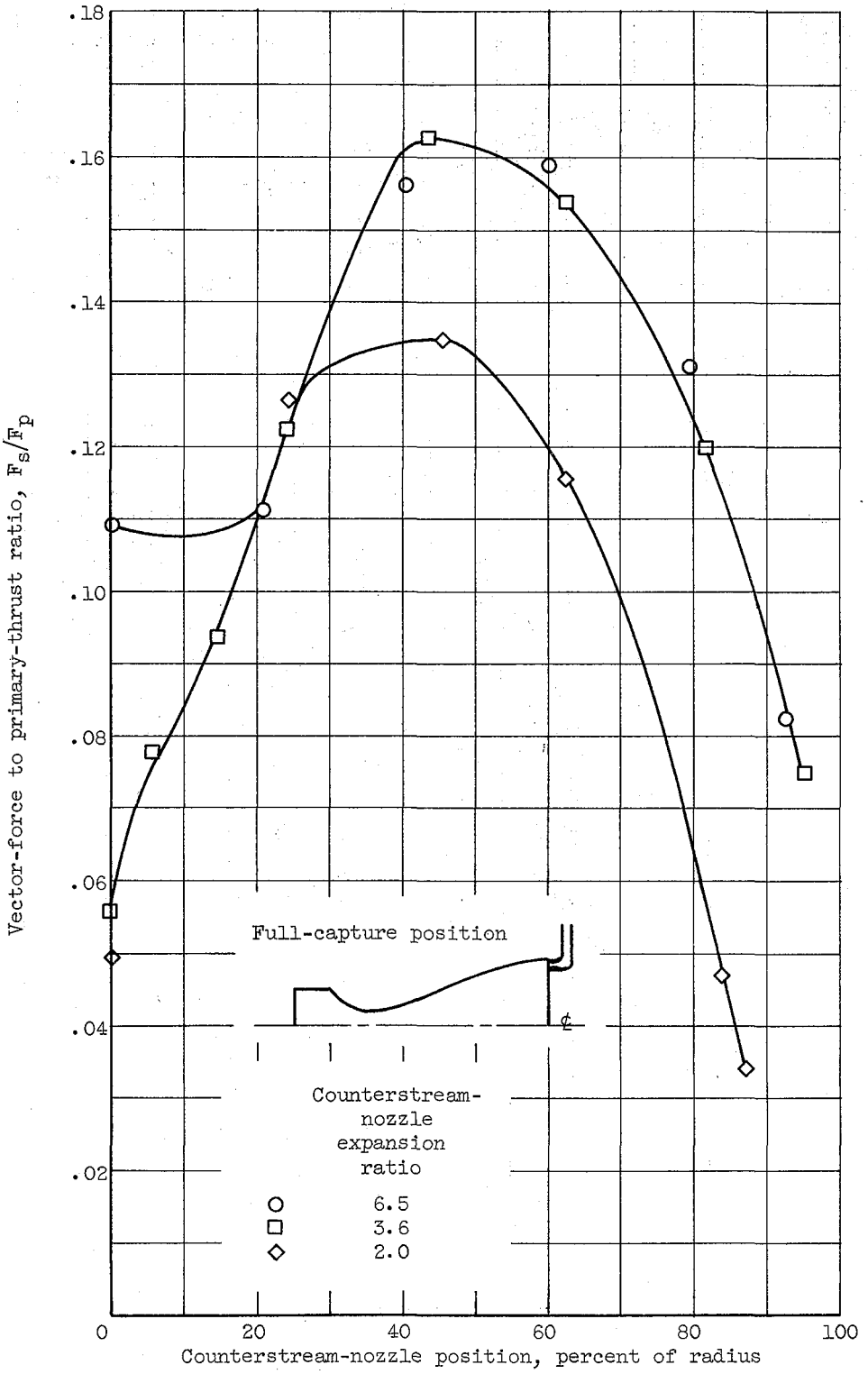

Figure 23. - Effect of counterstream-nozzle expansion ratio for high-pressure counterstream configurations.

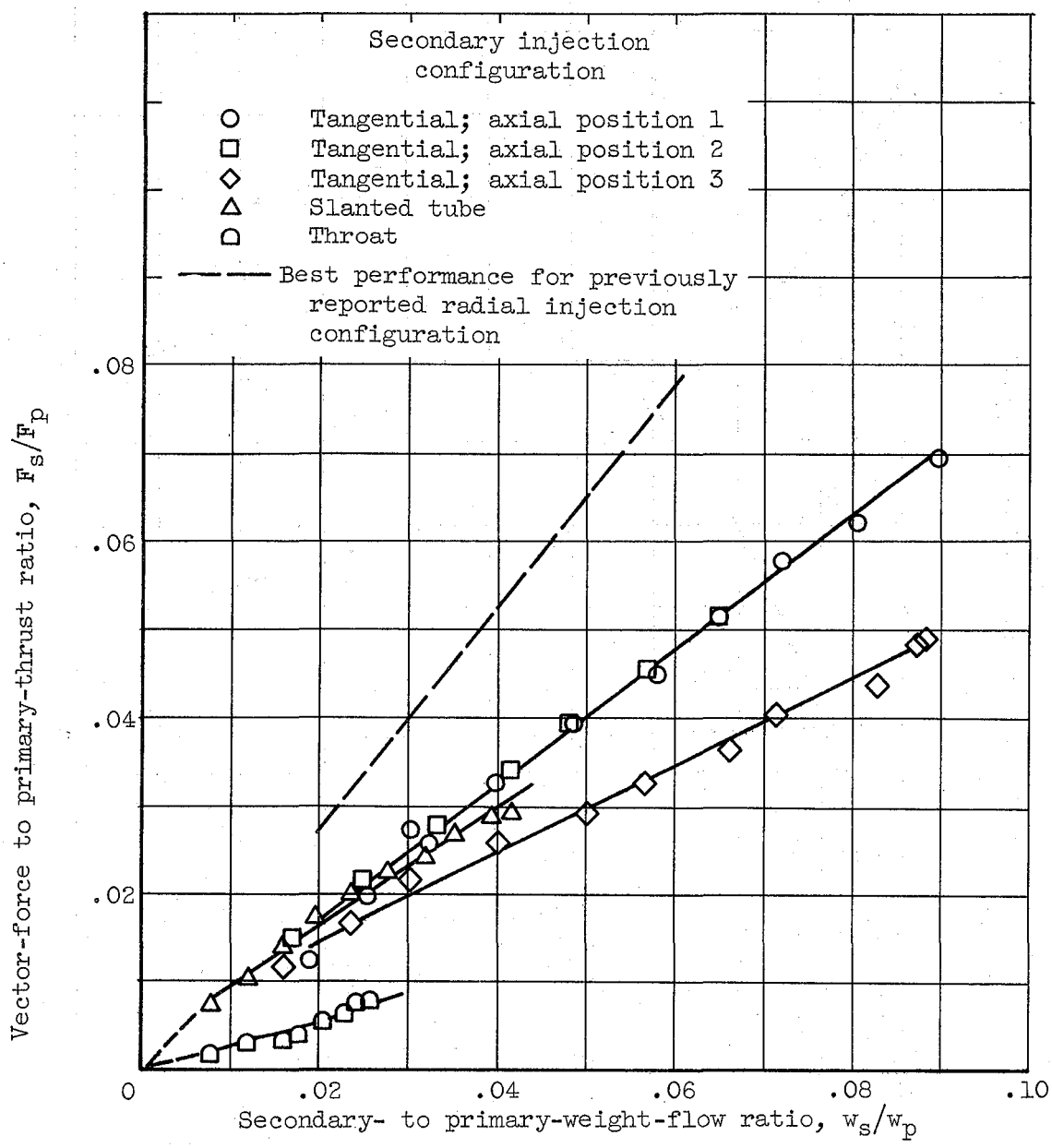

Figure 24. - Performance of miscellaneous vector-control configurations.

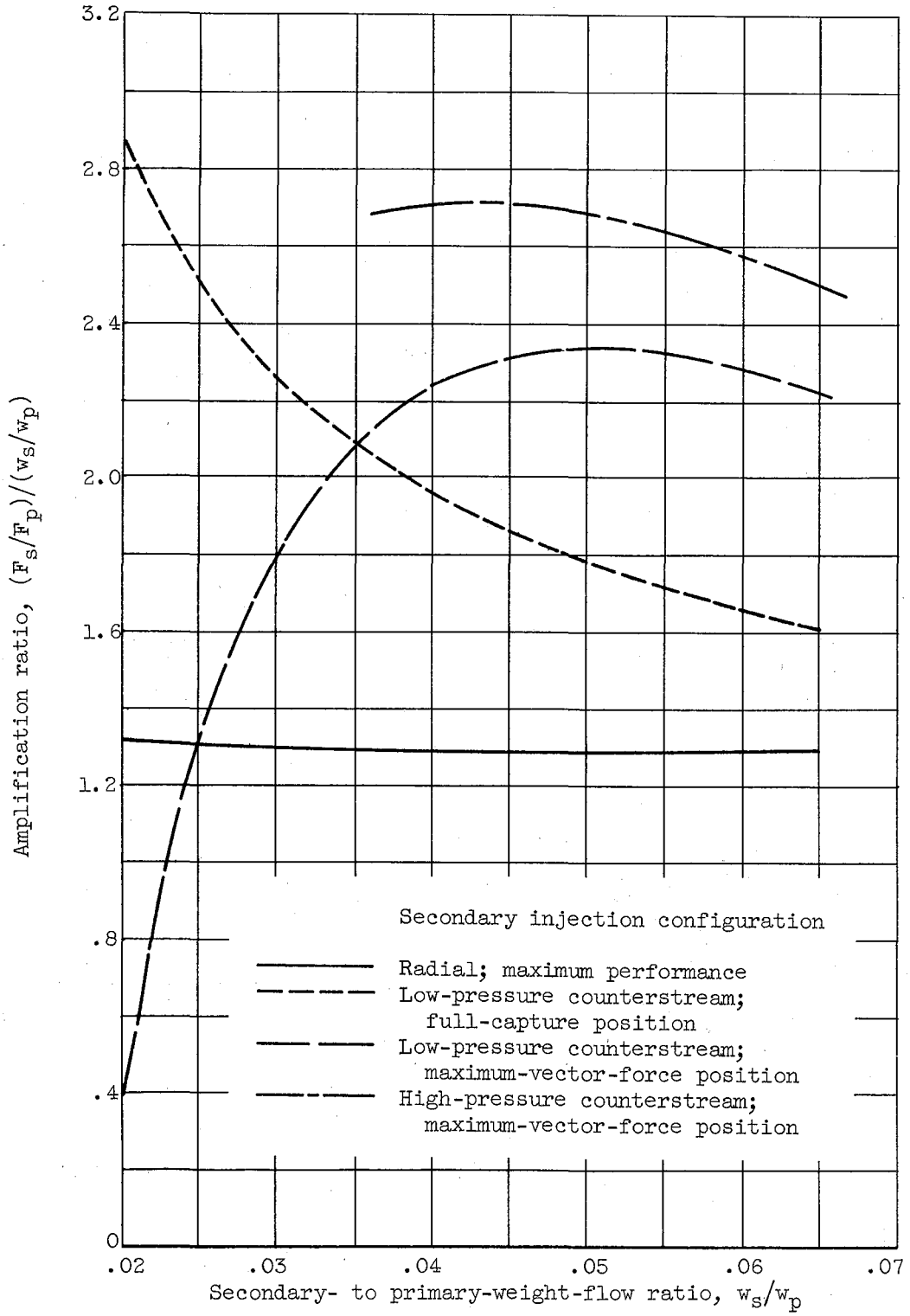

Figure 25. - Performance comparison of best vector-control configurations.

NASA - Langley Field, Va. E-992